# The JWST-SUSPENSE ultradeep spectroscopic program: survey overview and star formation histories of quiescent galaxies at 1 < z < 3

Slob, M.M.; Kriek, M.T.; Beverage, A.G.; Suess, K.A.; Barro, G.; Bezanson, R.; ... ; Weisz, D.R.

The Astrophysical Journal, 973:131 (23pp), 2024 October 01 https://doi.org/10.3847/1538-4357/ad65ff


# The JWST-SUSPENSE Ultradeep Spectroscopic Program: Survey Overview and Star Formation Histories of Quiescent Galaxies at $1 < z < 3$

Martje Slob[1], Mariska Kriek[1], Aliza G. Beverage[2], Katherine A. Suess[3,18], Guillermo Barro[4], Rachel Bezanson[7], Gabriel Brammer[5,6], Chloe M. Cheng[1], Charlie Conroy[8], Anna de Graaff[9], Natascha M. Förster Schreiber[10], Marijn Franx[1], Brian Lorenz[2], Pavel E. Mancera Piña[1], Danilo Marchesini[11], Adam Muzzin[12], Andrew B. Newman[13], Sedona H. Price[7], Alice E. Shapley[14], Mauro Stefanon[15,16], Pieter van Dokkum[17], and Daniel R. Weisz[2]

[1] Leiden Observatory, Leiden University, P.O. Box 9513, 2300 RA Leiden, The Netherlands; slob@strw.leidenuniv.nl
[2] Department of Astronomy, University of California, Berkeley, CA 94720, USA
[3] Kavli Institute for Particle Astrophysics and Cosmology and Department of Physics, Stanford University, Stanford, CA 94305, USA
[4] Department of Physics, University of the Pacific, Stockton, CA 90340, USA
[5] Cosmic Dawn Center (DAWN), Denmark
[6] Niels Bohr Institute, University of Copenhagen, Jagtvej 128, DK2200 Copenhagen N, Denmark
[7] Department of Physics and Astronomy and PITT PACC, University of Pittsburgh, Pittsburgh, PA 15260, USA
[8] Center for Astrophysics | Harvard & Smithsonian, Cambridge, MA 02138, USA
[9] Max-Planck-Institut für Astronomie, Königstuhl 17, D-69117, Heidelberg, Germany
[10] Max-Planck-Institut für extraterrestrische Physik, Giessenbachstrasse 1, D-85748 Garching, Germany
[11] Department of Physics & Astronomy, Tufts University, Medford, MA 02155, USA
[12] Department of Physics and Astronomy, York University, 4700 Keele Street, Toronto, ON MJ3 1P3, Canada
[13] Observatories of the Carnegie Institution for Science, 813 Santa Barbara Street, Pasadena, CA 91101, USA
[14] Department of Physics & Astronomy, University of California, Los Angeles, CA 90095, USA
[15] Departament d'Astronomia i Astrofísica, Universitat de València, C. Dr. Moliner 50, E-46100 Burjassot, València, Spain
[16] Unidad Asociada CSIC "Grupo de Astrofísica Extragaláctica y Cosmología" (Instituto de Física de Cantabria - Universitat de València), Spain
[17] Astronomy Department, Yale University, 52 Hillhouse Avenue, New Haven, CT 06511, USA
*Received 2024 April 18; revised 2024 July 15; accepted 2024 July 17; published 2024 September 26*

## Abstract

We present an overview and first results from the Spectroscopic Ultradeep Survey Probing Extragalactic Near-infrared Stellar Emission (SUSPENSE), executed with NIRSpec on JWST. The primary goal of the SUSPENSE program is to characterize the stellar, chemical, and kinematic properties of massive quiescent galaxies at cosmic noon. In a single deep NIRSpec/MSA configuration, we target 20 distant quiescent galaxy candidates ($z = 1$–3, $H_{\rm AB} \leqslant 23$), as well as 53 star-forming galaxies at $z = 1$–4. With 16 hr of integration and the G140M-F100LP dispersion-filter combination, we observe numerous Balmer and metal absorption lines for all quiescent candidates. We derive stellar masses ($\log M_*/M_\odot \sim 10.2$–11.5) and detailed star formation histories (SFHs) and show that all 20 candidate quiescent galaxies indeed have quenched stellar populations. These galaxies show a variety of mass-weighted ages (0.8–3.3 Gyr) and star formation timescales (∼0.5–4 Gyr), and four out of 20 galaxies were already quiescent by $z = 3$. On average, the $z > 1.75$ [$z < 1.75$] galaxies formed 50% of their stellar mass before $z = 4$ [$z = 3$]. Furthermore, the typical SFHs of the galaxies in these two redshift bins ($z_{\rm mean} = 2.2$ [1.3]) indicate that galaxies at higher redshift formed earlier and over shorter star formation timescales compared to lower redshifts. Although this evolution is naturally explained by the growth of the quiescent galaxy population over cosmic time, number density calculations imply that mergers and/or late-time star formation also contribute to the evolution. In future work, we will further unravel the early formation, quenching, and late-time evolution of these galaxies by extending this work with studies on their chemical abundances, resolved stellar populations, and kinematics.

*Unified Astronomy Thesaurus concepts:* Galaxy evolution (594); Galaxy quenching (2040); Galaxy formation (595)

*Materials only available in the online version of record: figure set, machine-readable tables*

## 1. Introduction

One of the most remarkable discoveries in extragalactic astronomy from the past two decades is the existence of a population of quiescent galaxies at $z \sim 2$ and beyond (e.g., Franx et al. 2003; Cimatti et al. 2004; Daddi et al. 2005; Kriek et al. 2006; Straatman et al. 2014; Glazebrook et al. 2017, 2024; Schreiber et al. 2018; Tanaka et al. 2019; Forrest et al. 2020a, 2020b; Esdaile et al. 2021; Carnall et al. 2023a, 2023b; Antwi-Danso et al. 2023; Valentino et al. 2023; Nanayakkara et al. 2024). The star formation rates (SFRs) of these galaxies are strongly suppressed, and their inferred star formation histories (SFHs) indicate that they formed their stars in vigorous bursts, followed by an efficient quenching process (e.g., Kriek et al. 2016; Carnall et al. 2019; Forrest et al. 2020a, 2020b; Jafariyazani et al. 2020; Valentino et al. 2020; Beverage et al. 2024a). Galaxy formation models struggle to create this galaxy population so early in the Universe's history (e.g., Schreiber et al. 2018; Cecchi et al. 2019; Gould et al. 2023;

[18] NHFP Hubble Fellow.

Hartley et al. 2023; Weller et al. 2024). Hence, the early and fast formation of these galaxies, as well as the cessation of star formation within them, has remained a problem.

Their subsequent evolution is also a puzzle. Distant quiescent galaxies are much more compact and denser than massive early-type galaxies in the present-day Universe (e.g., Daddi et al. 2005; van Dokkum et al. 2008; van der Wel et al. 2014; Suess et al. 2019, 2021). Studies also find that older quiescent galaxies have larger sizes (Whitaker et al. 2012; Yano et al. 2016; Almaini et al. 2017; Suess et al. 2020), though other results suggest the opposite trend with more compact quiescent galaxies having older stellar populations (Gargiulo et al. 2017; Wu et al. 2018; Hamadouche et al. 2022). Furthermore, in contrast to the majority of present-day quiescent galaxies, distant quiescent galaxies appear to have disklike morphologies (van der Wel et al. 2011; Chang et al. 2013) and may be rotationally supported (Toft et al. 2017; Newman et al. 2018; D'Eugenio et al. 2023). Two popular scenarios emerged to explain the observed evolution. In the first scenario, distant quiescent galaxies are the cores of present-day massive elliptical galaxies (e.g., Bezanson et al. 2009; Naab et al. 2009; van Dokkum et al. 2010), with their outer regions building up gradually over cosmic time through a series of minor mergers. This scenario can also explain how early quiescent disks evolved into the present-day massive elliptical galaxies, as minor mergers can gradually perturb the ordered rotation (Bournaud et al. 2007; Naab et al. 2014; Lagos et al. 2018). The minor merger scenario is also supported by the finding that color gradients increase with galaxy age (Suess et al. 2020) and that distant quiescent galaxies have many small companions (Newman et al. 2012; Suess et al. 2023). In a second popular scenario, the size evolution can be explained by the growth of the quiescent galaxy population, as galaxies that quench at later times are predicted to be larger (i.e., progenitor bias; e.g., Khochfar & Silk 2006; Carollo et al. 2013; Poggianti et al. 2013; Ji & Giavalisco 2022). Both scenarios are thought to play a role in the observed evolution (e.g., Belli et al. 2017).

However, more recent observations show that this picture may be too simplistic. First, neither progenitor bias nor minor mergers can explain the difference in [Fe/H] of 0.2–0.3 dex between distant quiescent galaxies and the cores of nearby early-type galaxies (Kriek et al. 2016, 2019; Carnall et al. 2022; Gu et al. 2022; Beverage et al. 2024a; Zhuang et al. 2023). Furthermore, while the cores of nearby massive early-type galaxies are found to have bottom-heavy initial mass functions (IMFs; Treu et al. 2010; Conroy & van Dokkum 2012), the IMF in distant quiescent galaxies appears more consistent with a Milky Way (i.e., Kroupa 2001; Chabrier 2003) IMF (Mendel et al. 2020; Forrest et al. 2022; Kriek et al. 2024). Thus, these observations imply that the evolution may be more complicated than initially proposed, and major mergers and/or late-time star formation may play a role as well.

In order to solve these puzzles and understand the early formation, quenching mechanism, and late-time evolution of the distant quiescent galaxy population, we need detailed stellar population, chemical, and kinematic properties of a significant sample of distant quiescent galaxies. Obtaining such measurements has been exceedingly challenging, as they rely on ultradeep rest-frame optical spectra. Consequently, the above spectroscopic studies are based on only a few very massive and/or lensed galaxies. Furthermore, despite extreme integration times with the most efficient near-infrared spectrographs on large ground-based telescopes, the spectra still have significant uncertainties and suffer from low spatial resolution. Thus, we have reached the limits of current ground-based facilities.

With the advent of JWST, we are finally capable of breaking this impasse. Early results have demonstrated the power of JWST to observe distant quiescent galaxies ($z \gtrsim 2.5$) with the low-resolution mode (Glazebrook et al. 2023; Marchesini et al. 2023; de Graaff et al. 2024b; Nanayakkara et al. 2024; Setton et al. 2024). Furthermore, using medium-resolution spectroscopy, Belli et al. (2024), D'Eugenio et al. (2023), and Carnall et al. (2023a) demonstrate the detection of primarily Balmer absorption lines in galaxies at $z = 2.445$, $z = 3.064$, and $z = 4.658$, respectively. While these studies attest to the unprecedented sensitivity of NIRSpec, they either lack the required spectral resolution or do not have sufficiently old galaxies to observe metal absorption lines. Such metal absorption lines allow us to study stellar populations and chemical abundances in unparalleled detail. Furthermore, the samples are still very small, and the quiescent galaxies found at $z > 3$ are likely not representative of the full massive quiescent galaxy population. Thus, the next step is to obtain larger, more representative, medium-resolution samples and target older quiescent galaxies, for which we can measure a range of metal absorption lines. Taking full advantage of the multiplexing capabilities of NIRSpec (Ferruit et al. 2022) for studying quiescent galaxies, however, remains challenging due to the low number densities of such galaxies; consequently, they are rare in spectroscopic surveys executed in the deep legacy fields.

To successfully overcome these challenges and obtain ultradeep, medium-resolution, rest-frame optical, spatially resolved spectra of a significant sample of distant quiescent galaxies, we are conducting the Cycle 1 Spectroscopic Ultradeep Survey Probing Extragalactic Near-infrared Stellar Emission (SUSPENSE) program. The SUSPENSE observations were collected with the JWST NIRSpec/MSA in 2024 January. SUSPENSE observes 20 quiescent galaxy candidates at $1 < z < 3$ in a single NIRSpec/MSA configuration. The spectra are of unprecedented depth and show a multitude of Balmer and metal absorption lines, and the micro-shutter assembly (MSA) slits extend over the full spatial range of the galaxies.

In this paper, we present an overview of the survey, the observational strategy, the data reduction and analysis, the sample characteristics, and the SFHs of 20 quiescent galaxies in our sample. The paper is organized as follows. In Section 2, we present the SUSPENSE survey design and observing strategy. In Section 3, we discuss the two-dimensional (2D) data processing and the extraction of the one-dimensional (1D) spectra. Section 4 describes the stellar population fitting, the sample characteristics, and the SFHs of the quiescent galaxy sample. In Section 5, we discuss the implications of our findings for the evolution of the quiescent galaxy population. Finally, in Section 6, we present a summary.

Throughout this work, we assume a Lambda cold dark matter ($\Lambda$CDM) cosmology with $\Omega_m = 0.3$, $\Omega_\Lambda = 0.7$, and $H_0 = 70\,\mathrm{km\,s^{-1}\,Mpc^{-1}}$ and the solar abundances of Asplund et al. (2009) with $Z_\odot = 0.0142$. All magnitudes are given in the AB magnitude system (Oke & Gunn 1983).

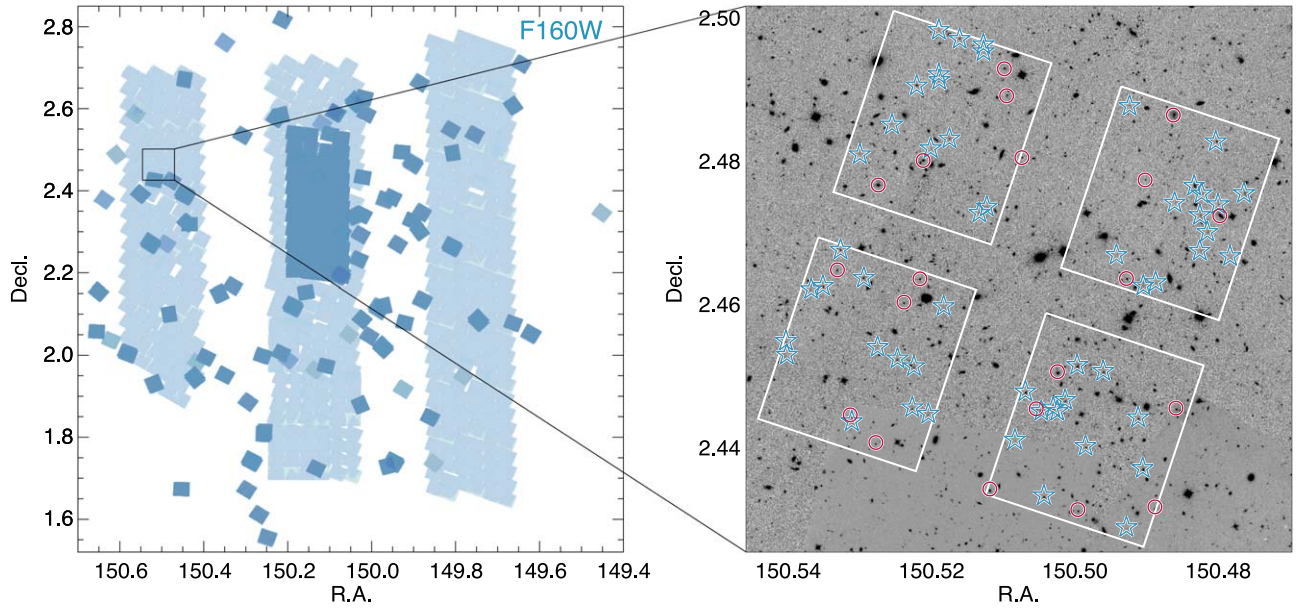


**Figure 1.** Footprint of the SUSPENSE observations in the larger COSMOS field. The left panel shows the weight map of all available public Hubble Space Telescope (HST)/F160W imaging, constructed as part of the COSMOS-DASH program (Momcheva et al. 2017). The darker blue central contiguous area represents the CANDELS survey (Grogin et al. 2011; Koekemoer et al. 2011), and the three larger and lighter stripes represent the shallower COSMOS-DASH survey, which overlaps with the deep UltraVISTA stripes. In the right panel, we zoom in on our pointing, now showing the combined F160W image and the footprint of the NIRSpec/MSA. The red circles and blue stars indicate the quiescent and star-forming targets, respectively.

## 2. Observations

### 2.1. Target Selection and MSA Configuration

The JWST-Cycle 1 SUSPENSE program (ID 2110) aims to characterize the stellar, chemical, and kinematic properties of the distant quiescent galaxy population. To reach this goal, we require ultradeep rest-frame optical spectra of a significant sample of distant quiescent galaxies. The NIRspec MSA's unparalleled sensitivity and multiplexing capabilities make it ideally suited to this task. However, fully utilizing its multiplexing capabilities depends on identifying a field with a high density of these galaxies.

To this end, we used the large overlapping area of the UltraVISTA (McCracken et al. 2012; Muzzin et al. 2013a), COSMOS (F814W; Scoville et al. 2007) and COSMOS-DASH (F160W; Momcheva et al. 2017; Mowla et al. 2019; Cutler et al. 2022) surveys to optimize our pointing. We first identified all $z_{\rm phot} > 1.1$ quiescent galaxies in the UltraVISTA DR3 catalog (Muzzin et al. 2013b) using the *UVJ* selection criteria by Muzzin et al. (2013a). The redshift criterion ensured that we observe at least two Balmer lines for all targets. We additionally required $H < 22.6$, such that the galaxies are sufficiently bright for resolved kinematic and elemental abundance studies. We identified an extraordinary pointing for which we observe ∼20 such galaxies in one NIRSpec/MSA configuration.

We rederived and updated the coordinates of all galaxies and stars in our pointing by running SExtractor (Bertin & Arnouts 1996) on the COSMOS-DASH F160W image. For the galaxies, we used the brightest pixel positions, while for the stars, we used the barycenter positions. For the fainter galaxies that were not detected in F160W (all 20 candidate quiescent galaxy targets are detected), we used the original UltraVISTA coordinates.

We used the Astronomer's Proposal Tool (APT) MSA planning tool to design two nearly identical MSA configurations, offset in dispersion direction by eight shutters. We assumed the assigned position angle of 71.6174°, three shutter slitlets, and a three-nod pattern (though we only use the two outer nod positions, as discussed in the next section). As our quiescent galaxy candidates are extended, we used the "unconstrained" (midbar) option for the source centering constraint, implying that our galaxies may be centered behind both the horizontal and vertical MSA bars. While this was the case for five of the quiescent targets, most galaxies were centered in the open-shutter area. We also allowed galaxies in areas of the detector that are affected by failed open shutters.

Within the group of quiescent galaxies, the highest priority was given to galaxies at $z \geqslant 1.5$, followed by $1.3 \leqslant z < 1.5$ and $1.1 \leqslant z < 1.3$. After we identified our optimal configuration, we extended the slitlets by one microshutter, where possible. Next, we added filler targets by hand, prioritizing bright star-forming galaxies at $z \sim 1.5$, for which we expect to detect bright stellar continuum emission and all Balmer emission lines, as well as fainter quiescent galaxies ($H > 22.6$). Eventually, we considered all targets with $z > 1.1$. In contrast to the primary targets, we did not require the filler galaxies to have coverage in all nod and dither positions. Finally, after no more targets could be added, we extended more slits and opened microshutters on empty sky to construct a master background. For our quiescent targets, the slitlets range from three to seven microshutters, with an average of five. The slit lengths of the others targets varied between one and seven shutters. Due to failed closed shutters in the MSA, we could not open the exact same shutters in the two dithered configurations for all targets, which means that for some targets, the number of shutters in a slitlet differs between the two dithers.

In total, we target 73 galaxies, of which 20 are quiescent galaxy candidates. In Figure 1, we show our pointing within the larger COSMOS area, as well as the footprint of the NIRSpec/MSA and the targeted galaxies.

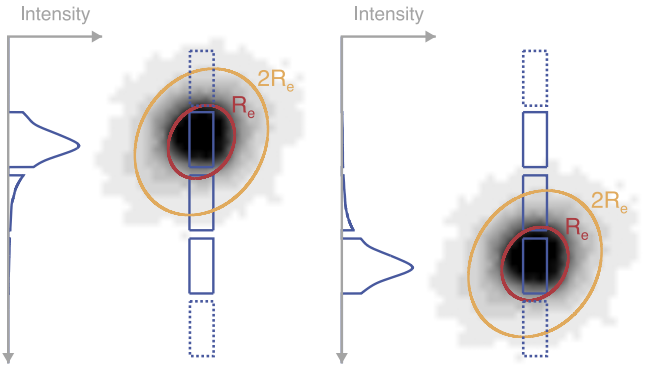


**Figure 2.** Nod pattern shown for a massive $z \sim 2.1$ quiescent galaxy with an $R_e$ of 2.67 kpc (Kriek et al. 2016). The image is taken with HST/F160W from CANDELS. The red ellipsoid contains half of the light (for the NIRSpec PSF), while the orange ellipsoid indicates the extent of two half-light radii ($R_e$). The profiles on the left of the images show the light distribution within the shutters. This figure illustrates that the galaxies extend beyond a single shutter and thus a two-shutter nod is required to minimize self-subtraction of the galaxy's signal in the standard sky subtraction.

### 2.2. Observing Strategy

Our program was executed on 2024 January 2 and 4, employing the NIRSpec/MSA along with the G140M-F100LP dispersion-filter combination. The wavelength coverage for this setting is 0.97–1.84 $\mu$m, with a spectral resolution of $R \sim 1000$. This wavelength range corresponds to a rest-frame wavelength coverage of ∼3700–7000 Å for our median redshift ($z \sim 1.5$). Though the exact rest-frame wavelength coverage depends on the redshift, for most quiescent galaxies, we observed 4600–5400 Å, which includes Mg I at 5178 Å as well as several prominent Fe I lines. Furthermore, all spectra cover at least one Balmer line.

We used a two-point nod pattern with a cross-dispersion offset of two microshutters, corresponding to an angular offset of 1.″06. This angular offset translates to a distance of 8.6–9.0 kpc at the targeted redshift. This offset was strategically chosen based on the typical sizes of quiescent targets at our targeted redshift range; with half-light radii of up to ∼3 kpc (Cutler et al. 2022), a two-microshutter offset facilitates the use of the adjacent offset frames as sky, as illustrated in Figure 2. A cross-dispersion offset of just one microshutter, as used in the majority of NIRSpec/MSA studies of distant galaxies, would have resulted in a partial self-subtraction of the signal during the standard reduction procedure.

We observed our galaxies in two different configurations, offset by eight microshutters in the dispersion direction. This dither, combined with the two-point nod pattern, resulted in four offset positions, needed to adequately mitigate detector and microshutter defects. Finally, our two offset MSA configurations reduce the detector gap, as the two dithers resulted in spectra that were shifted in the dispersion direction by ∼130 Å.

Because of microshutter defects, it was not possible to observe exactly the same galaxies in all four positions. Thirty-four galaxies have full coverage, including 18 quiescent targets (see Table 1). Two quiescent galaxies only have partial coverage, either because they were on the edge of the detector (130183) or because they were not prioritized, as they are faint (129966). In total, four galaxies have ∼75% coverage, 22 galaxies have ∼50% coverage, and 13 galaxies have ∼25% coverage.

Our observations were split over two identical visits. For both target acquisitions, we used the MSATA method and six alignment stars. After the acquisition, we took a confirmation image of 379 s of the first configuration. During each visit, we observed both dither configurations. For both configurations, we took 10 integrations of 1473 s each, with 20 groups per integration and the NRSIRS2 readout pattern. We nodded to a new position after two exposures; thus, for each dither configuration per visit, we have five nod positions. The total integration time per configuration per visit is 14,730 s. Combining both visits and configurations, we have a total on-source integration time of 16.4 hr.

## 3. Reduction and Data Overview

### 3.1. Data Reduction

We reduced the data using a modified version of the JWST Science Calibration Pipeline (Bushouse et al. 2023) v1.12.5 and version 1183 of the Calibration Reference Data System (CRDS). Since the two dithers in our observations have slightly different MSA configurations, we reduce the dithers separately and combine the resulting 1D spectra. Below, we describe the main data reduction steps and our modifications to the standard JWST Calibration Pipeline.

In Stage 1 of the JWST Calibration Pipeline, the master bias frame and dark current were subtracted, and detector artifacts were removed. To remove large cosmic-ray events (snowballs), we set `expand_large_events = True`, `min_sat_area = 15`, and `min_jump_area = 15` in the `jump` step. The pipeline then flags saturated pixels, removes jumps due to cosmic rays, and obtains the count-rate frames by fitting the slope of each pixel.

After Stage 1 of processing, the count-rate frames still contain $1/f$ correlated vertical readout noise (Schlawin et al. 2020). We remove this noise using the correction algorithm from `grizli` (Brammer 2023). In Stage 2 of the JWST Calibration Pipeline, the background subtraction for the entire detector of each count-rate frame is performed. Using the pipeline, we construct the background for each frame by taking the average of all frames that were observed during the same visit and dither but are in the opposite nodding position of our two-nod pattern. After background subtraction, the 2D spectra associated with our targets were cut out from the full detector frame, and a flat-field, path-loss, and bar-shadow correction was applied to each individual 2D spectrum. Since our sources are extended with respect to the shutter size, we use the CRDS path-loss calibration file corresponding to a uniformly illuminated slit. The fluxes of the corrected 2D spectra were then calibrated to convert the data from count-rate units to surface brightness.

In Stage 3, the pipeline combines the frames of all nods and observing days for each target. In order to combine the individual frames, the 2D spectra were first rectified and resampled to a common reference frame. Next, we identified outlier pixels caused by additional cosmic-ray impacts or bad pixels in the individual frames of each target using the outlier detection algorithm from `MSAEXP` instead of the standard JWST Calibration Pipeline outlier removal algorithm.[19] While masking outliers, we combined the rectified 2D frames for both nods and visits by weighing each pixel by its inverse read noise to construct the final 2D spectrum for each dither. We then used the Horne (1986) optimal extraction algorithm to get the 1D spectra for each dither position. We rescale the 1D spectra to

[19] https://github.com/gbrammer/msaexp

**Table 1**
Overview of Parameters of the Quiescent Galaxy Candidate Sample

| ID | Coordinates | | $H$ | $z_{spec}$ | Rest-frame colors | | Prospector Fitting Parameters | | | | $t_{exp}$ |
|---|---|---|---|---|---|---|---|---|---|---|---|
| | R.A. (hh:mm:ss) | Decl. (dd:mm:s) | (mag) | | $U-V$ | $V-J$ | log $M_*$[a] ($M_\odot$) | log SFR ($M_\odot$ yr$^{-1}$) | Age[b] (Gyr) | log $Z_*$ ($Z_\odot$) | (hr) |
| 127345 | 10:02:02.85 | 2:26:03.4 | 21.3 | 1.168 | 1.85 | 0.97 | $10.72^{+0.00}_{-0.01}$ | $-2.79^{+0.38}_{-0.61}$ | $2.87^{+0.02}_{-0.05}$ | $-0.06^{+0.01}_{-0.00}$ | 16.4 |
| 130040 | 10:02:06.58 | 2:28:36.2 | 20.4 | 1.170 | 2.03 | 1.33 | $11.21^{+0.01}_{-0.01}$ | $-1.97^{+0.91}_{-2.46}$ | $2.71^{+0.04}_{-0.04}$ | $-0.30^{+0.03}_{-0.03}$ | 16.4 |
| 128452[c,d] | 10:02:00.58 | 2:27:02.4 | 20.5 | 1.205 | 1.63 | 0.99 | $10.99^{+0.01}_{-0.00}$ | $0.50^{+0.01}_{-0.01}$ | $2.41^{+0.09}_{-0.08}$ | $-0.39^{+0.01}_{-0.01}$ | 16.4 |
| 127154 | 10:01:57.32 | 2:25:54.5 | 21.2 | 1.205 | 1.92 | 1.01 | $10.75^{+0.01}_{-0.01}$ | $-4.07^{+1.56}_{-5.75}$ | $2.35^{+0.06}_{-0.07}$ | $-0.22^{+0.02}_{-0.02}$ | 16.4 |
| 130208 | 10:02:05.08 | 2:28:48.5 | 20.8 | 1.231 | 1.71 | 0.80 | $10.95^{+0.00}_{-0.00}$ | $-3.32^{+1.15}_{-4.89}$ | $3.26^{+0.02}_{-0.03}$ | $-0.76^{+0.01}_{-0.01}$ | 16.4 |
| 129982 | 10:01:55.14 | 2:28:20.7 | 20.3 | 1.249 | 1.73 | 1.18 | $11.22^{+0.01}_{-0.01}$ | $0.97^{+0.02}_{-0.02}$ | $2.49^{+0.04}_{-0.05}$ | $-0.38^{+0.02}_{-0.02}$ | 13.1 |
| 127108 | 10:01:59.90 | 2:25:53.1 | 22.5 | 1.335 | 1.63 | 0.84 | $10.24^{+0.02}_{-0.03}$ | $-1.23^{+0.28}_{-0.97}$ | $2.11^{+0.10}_{-0.10}$ | $-0.34^{+0.06}_{-0.07}$ | 16.4 |
| 129197[d] | 10:02:07.95 | 2:27:53.5 | 22.3 | 1.474 | 1.88 | 1.07 | $10.52^{+0.02}_{-0.02}$ | $-2.52^{+1.15}_{-3.71}$ | $1.73^{+0.11}_{-0.10}$ | $0.17^{+0.01}_{-0.02}$ | 16.4 |
| 130647[c] | 10:01:56.70 | 2:29:11.3 | 20.1 | 1.508 | 1.74 | 1.08 | $11.49^{+0.00}_{-0.00}$ | $0.48^{+0.02}_{-0.02}$ | $3.18^{+0.01}_{-0.01}$ | $-0.15^{+0.03}_{-0.02}$ | 16.4 |
| 130934[c,d] | 10:02:02.36 | 2:29:34.6 | 21.9 | 1.565 | 1.57 | 1.08 | $10.60^{+0.05}_{-0.04}$ | $0.97^{+0.08}_{-0.06}$ | $2.17^{+0.33}_{-0.19}$ | $-0.55^{+0.06}_{-0.09}$ | 16.4 |
| 129149 | 10:01:58.27 | 2:27:49.2 | 21.2 | 1.579 | 1.78 | 0.93 | $11.02^{+0.01}_{-0.01}$ | $-2.76^{+1.17}_{-4.87}$ | $1.82^{+0.07}_{-0.10}$ | $0.18^{+0.01}_{-0.01}$ | 16.4 |
| 130183[c] | 10:02:01.77 | 2:28:49.9 | 22.2 | 1.757 | 1.62 | 1.06 | $10.78^{+0.04}_{-0.04}$ | $0.77^{+0.21}_{-0.66}$ | $1.09^{+0.21}_{-0.24}$ | $-1.37^{+0.10}_{-0.02}$ | 6.6 |
| 128041 | 10:01:56.61 | 2:26:44.1 | 21.9 | 1.760 | 1.42 | 0.97 | $10.71^{+0.01}_{-0.01}$ | $-0.38^{+0.21}_{-0.20}$ | $1.79^{+0.04}_{-0.03}$ | $-0.37^{+0.07}_{-0.06}$ | 16.4 |
| 127700 | 10:02:06.66 | 2:26:26.8 | 22.6 | 2.013 | 1.62 | 1.11 | $10.92^{+0.03}_{-0.05}$ | $0.60^{+0.08}_{-0.11}$ | $1.81^{+0.15}_{-0.11}$ | $-0.35^{+0.15}_{-0.20}$ | 16.4 |
| 129133 | 10:02:05.19 | 2:27:49.0 | 22.1 | 2.139 | 1.73 | 1.10 | $11.09^{+0.02}_{-0.02}$ | $-0.31^{+0.32}_{-0.52}$ | $1.47^{+0.06}_{-0.05}$ | $-0.46^{+0.04}_{-0.05}$ | 16.4 |
| 127941 | 10:02:07.52 | 2:26:40.7 | 22.5 | 2.141 | 1.55 | 1.14 | $10.80^{+0.02}_{-0.02}$ | $0.22^{+0.15}_{-0.16}$ | $1.72^{+0.02}_{-0.02}$ | $-0.24^{+0.03}_{-0.02}$ | 16.4 |
| 128036 | 10:02:01.29 | 2:26:43.8 | 22.2 | 2.196 | 1.49 | 0.87 | $10.92^{+0.04}_{-0.03}$ | $-0.99^{+0.64}_{-2.65}$ | $1.11^{+0.05}_{-0.05}$ | $0.08^{+0.04}_{-0.04}$ | 16.4 |
| 128913 | 10:02:05.72 | 2:27:37.3 | 22.6 | 2.285 | 1.68 | 0.89 | $10.91^{+0.03}_{-0.03}$ | $-3.70^{+2.13}_{-9.49}$ | $1.71^{+0.11}_{-0.42}$ | $-0.94^{+0.82}_{-0.10}$ | 16.4 |
| 130725[d] | 10:02:02.28 | 2:29:21.0 | 22.2 | 2.692 | 1.33 | 0.96 | $11.09^{+0.05}_{-0.02}$ | $0.10^{+0.41}_{-0.26}$ | $1.17^{+0.03}_{-0.03}$ | $0.15^{+0.03}_{-0.06}$ | 16.4 |
| 129966 | 10:01:57.65 | 2:28:38.7 | 23.2 | 2.923 | 1.45 | 0.81 | $10.91^{+0.04}_{-0.04}$ | $0.61^{+0.27}_{-0.39}$ | $0.79^{+0.07}_{-0.06}$ | $0.01^{+0.10}_{-0.10}$ | 4.9 |

**Notes.** The derivation of the coordinates is described in Section 2.1, the rest-frame $U-V$ and $V-J$ colors are obtained in Section 4.3, and the measurements of the spectroscopic redshifts and Prospector fitting parameters are described in Section 4.1.
[a] Surviving stellar mass.
[b] Mass-weighted ages.
[c] Galaxies with a PSB best-fit SFH.
[d] Galaxies observed in a failed open-shutter area.

(This table is available in machine-readable form in the online article.)

the overlapping photometry (UVISTA $Y$, $J$, and $H$ bands) with a multiplicative factor calculated from the median spectrum and photometry. This rescaling accounts for the slit loss caused by the fact that our extended targets partly fall outside of the shutter, which is not properly corrected for in the path-loss correction step in the reduction pipeline. We only apply this scaling to sources with sufficiently strong continuum emission, including all quiescent galaxies. For the star-forming galaxies for which we only detect emission lines, we will properly account for the absolute flux calibration in future work.

Finally, we combine the 1D spectra for both dither positions. For spectra that are dispersed over both NIRSpec detectors, there is a wavelength gap in the spectrum caused by the separation of the two detectors. Our eight-shutter dither in the dispersion direction shifts this detector gap by ∼130 Å between the two dither positions, so that the detector gap is partly filled up in the combined spectrum. The spectrum at the edges of the detector gap is thus constructed from only one of the dithered spectra. We created a mask for each spectrum, indicating the bad pixels and spectral coverage. Finally, we weighed all unmasked pixels in the spectra by their on-source integration time to combine them into the final 1D spectrum.

### 3.2. Data Overview

We show an overview of the rest-frame normalized 1D spectra for all 20 quiescent targets in Figure 3, ordered by spectroscopic redshift (see Section 4.1). In Figure 4, we present the detailed observed-frame 1D spectra (bottom-right panels), 2D spectra for both dither positions (top-right panels), UltraVISTA photometry (bottom-left panels), and the F160W image from COSMOS-DASH (Mowla et al. 2019) for two example galaxies. We also show the position of the NIRSpec MSA shutters for the first nod on the image. The spectra of all quiescent galaxies in the sample are available as a figure set.

The rest-frame 1D spectra in Figure 3 show that we observe multiple Balmer absorption lines (green dotted lines) for nearly all quiescent targets, and the Mg I absorption line (red dotted line) is observed for 16 of our targets. Two of our quiescent targets are at too low redshifts to capture the targeted Mg I line, and for two galaxies, the line falls in the detector gap. For the 12 highest-redshift targets, we observe the 4000 Å break region, including the two Ca II lines (red). Additionally, we detect Na I, Fe I, and carbon $G$-band absorption lines for the majority of targets. For some quiescent targets, we also detect emission lines; for seven sources with rest-frame coverage below 3800 Å, we observe [O II] $\lambda\lambda$3727,3730 emission. Furthermore, for seven of the galaxies, we also observe [N II] $\lambda\lambda$6550,6585, [O III] $\lambda\lambda$4960, 5000, and/or Balmer emission lines. These emission lines in quiescent galaxies are thought to originate either from active galactic nuclei (AGN) or hot evolved stars (e.g., Yan et al. 2006; Belfiore et al. 2016; Belli et al. 2021; Maseda et al. 2021). Furthermore, the emission line

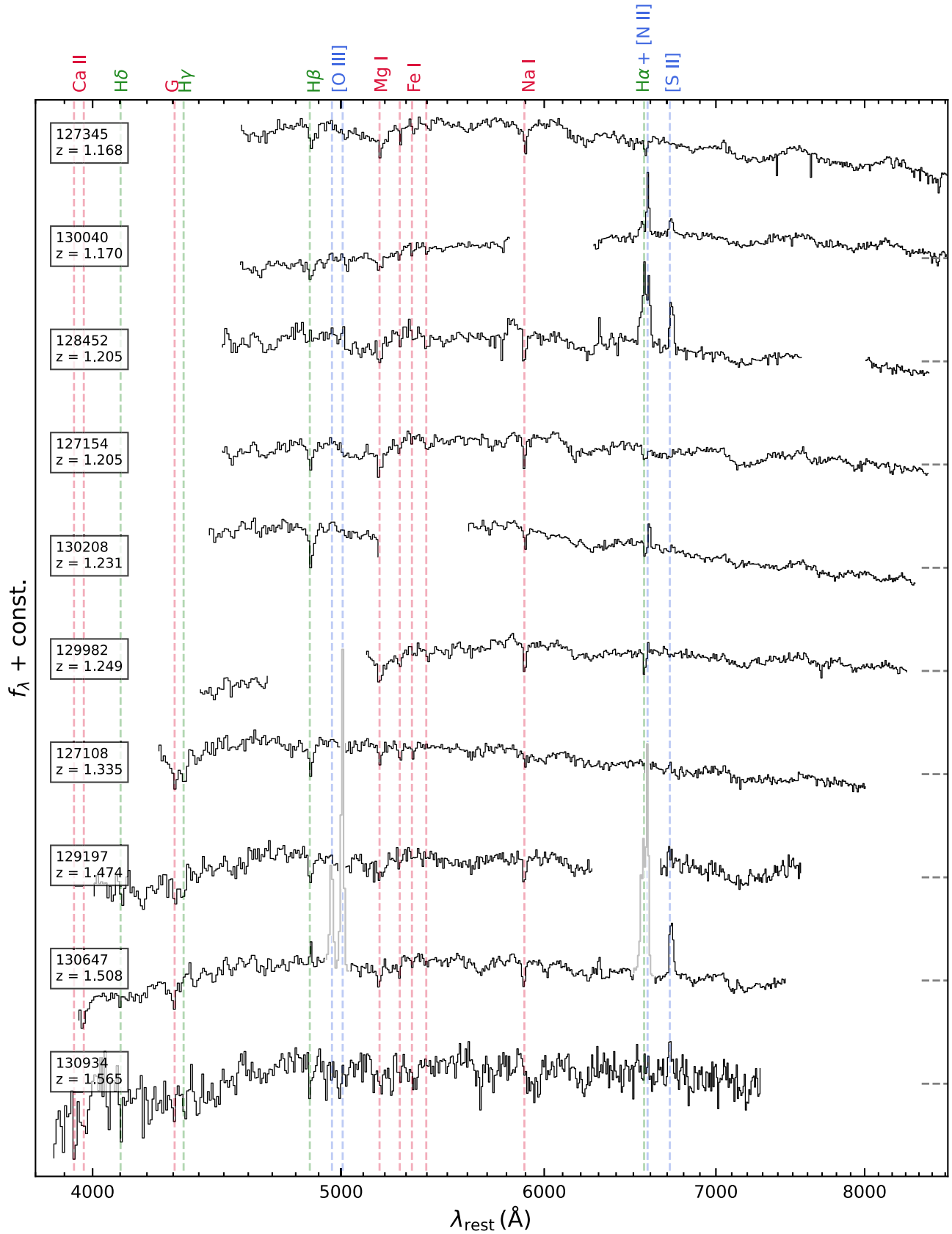


**Figure 3.** NIRSpec rest-frame spectra for our sample of 20 candidate quiescent galaxies, sorted by redshift and offset by a constant in the *y*-direction. We median bin the spectra over 3 pixels. Dashed blue, red, and green lines mark prominent emission, absorption, and Balmer features, respectively. For clarity purposes, strong emission lines overlapping with other spectra are displayed in gray. The dashed gray lines on the right indicate the zero-points of the spectra.

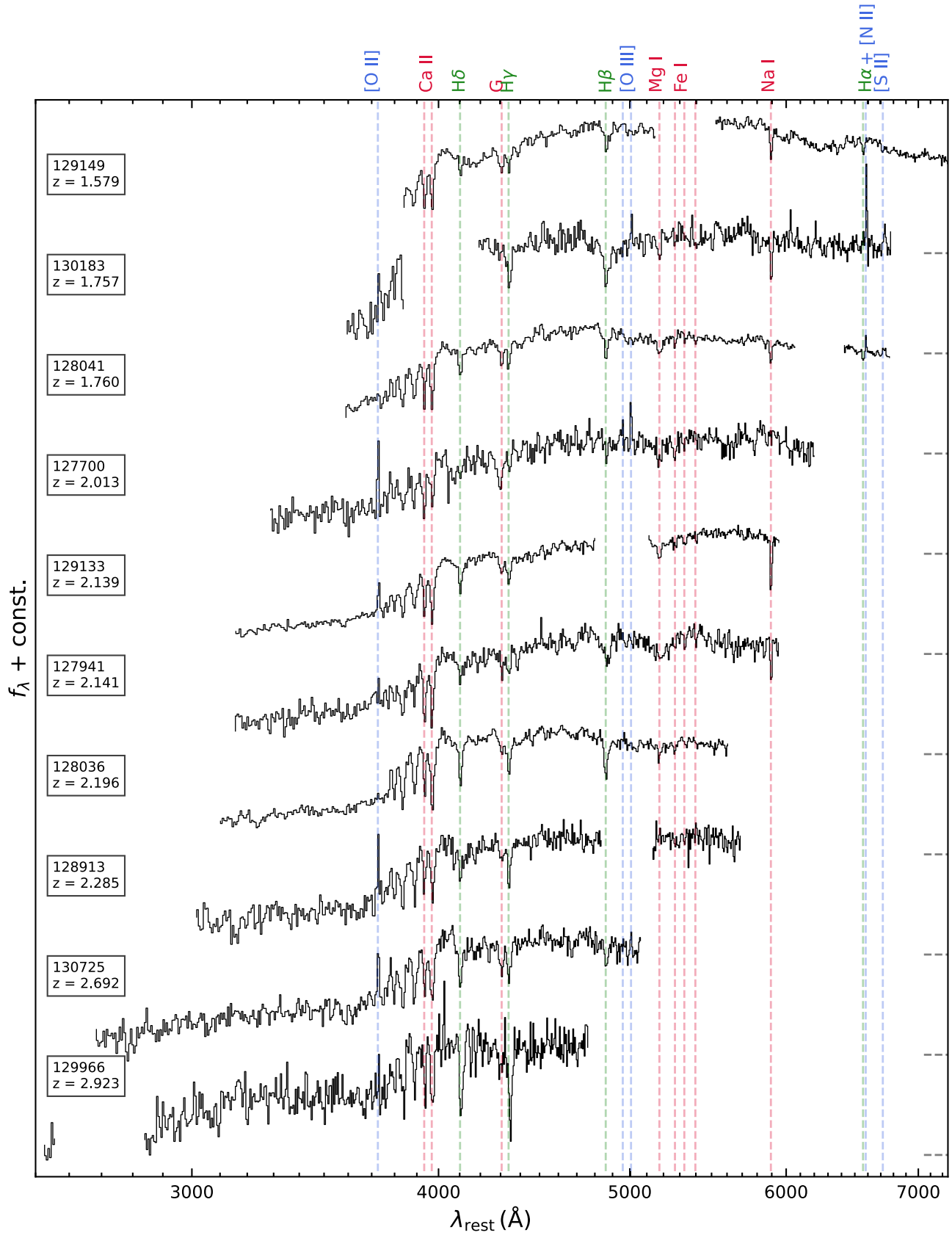


**Figure 3.** (Continued.)

ratios ([N II]/H$\alpha$, [O III]/H$\beta$) are also indicative of a non-star-forming origin. Thus, these lines likely originate from ionization by an AGN, shocks, or post–asymptotic giant branch (AGB) stars (e.g., Yan & Blanton 2012). A detailed investigation into the origin of these emission features will be the subject of a future study.

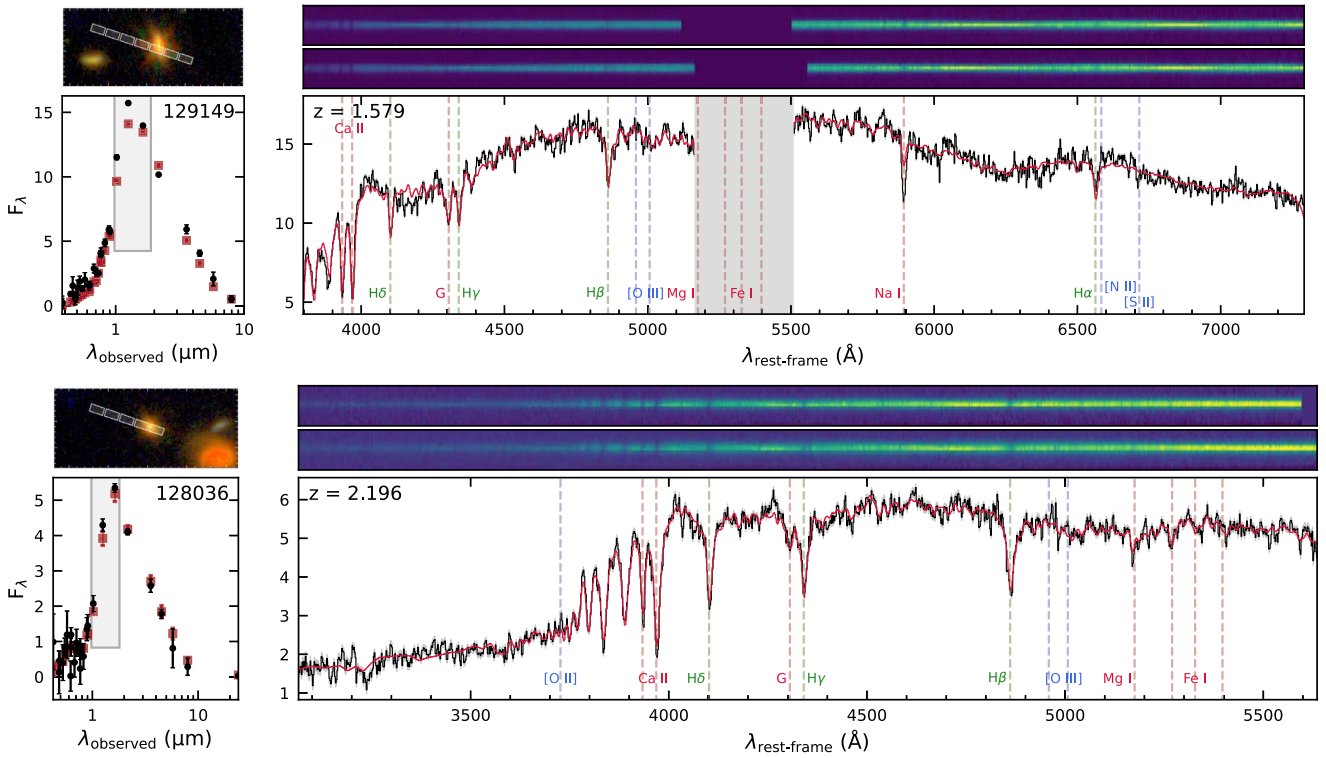


**Figure 4.** Overview of UltraVISTA photometric SEDs (bottom left), NIRSpec spectra (right), and JWST COSMOS-Web red, green, and blue (RGB) imaging (top left; Casey et al. 2023) of two example quiescent galaxies in our survey. The 2D spectra for the two observed dithers and the combined 1D spectrum are shown in the top-right and bottom-right panels, respectively. Flux densities ($F_\lambda$) are in $10^{-19}$ erg s$^{-1}$ cm$^{-2}$ Å$^{-1}$. The coverage of the NIRSpec spectra is indicated in the SED panels by the gray rectangles. The best-fit `Prospector` models to the photometry and spectra are shown in red (see Section 4.1). The images in the top-left panels show the COSMOS-Web RGB imaging, constructed from the F115W, F277W, and F444W filters (Casey et al. 2023), with an overlay of the NIRSpec MSA slit orientation for one nod position. The spectra of all quiescent galaxies in the sample (20 images) are available as a figure set.

(The complete figure set (20 images) is available.)

In Figure 5, we plot the median signal-to-noise ratio (SNR) per rest-frame Å between 4600 and 4800 Å as a function of rest-frame $V$-band magnitude. We use this spectral range to compute the SNR as all quiescent targets cover this wavelength region, and it captures no strong emission or absorption features that will bias the calculated SNR for individual galaxies. Overall, the targets that are brightest in the rest-frame $V$ band also have the highest SNRs, but for some targets, the signal is lower than expected based on their magnitude. For the two sources that were not covered by all four nod/dither configurations (indicated with cross symbols), the lower SNR can be explained from their lower on-source integration time. Next, to include more quiescent targets in our sample, we allowed objects to fall in areas of the detector that are affected by stray light from failed open shutters in the MSA. These targets are indicated with a plus symbol and indeed have lower SNRs than sources of a comparable magnitude.

Additionally, to further maximize our sample size, we allowed sources to fall anywhere in a shutter when designing the mask, including behind the bars separating neighboring shutters. In the right panel of Figure 5, we show an MSA shutter with the projected positions of the central coordinates of our quiescent targets, plotted using the same symbols as in the left panel.

From this panel, we conclude that most of the sources with relatively low SNR lie at the edge of the shutters or behind the shutter bars. For these less optimally centered sources, a large fraction of their light is not captured in the shutter, while the measured $V$-band flux is calculated using the galaxy's entire profile. However, since the typical size of quiescent galaxies in our redshift range at a rest-frame wavelength of ∼5000 Å is ∼2 kpc (Cutler et al. 2022), our targets are sufficiently extended to reach SNRs >10 for all sources (with full coverage and not affected by the open-shutter areas) that are at the shutter edges. We also note that the difference in redshifts, sizes, Sérsic indices, and alignment of our objects will increase the scatter in our SNRs, since the luminosity and observed fraction of each galaxy will differ.

In summary, the observed SNRs show that our choices for designing the MSA mask affected the obtained flux levels of our spectra. Nonetheless, the final SNRs ($\gtrsim$10) we obtain are sufficient for the goals of this survey. If we had been more conservative in the mask design by not allowing sources to fall behind the shutter bars and not using shutters affected by failed open shutters, our sample would have decreased from 20 to 11 quiescent targets. Overall, this shows that by allowing more flexibility in the mask design, we have greatly increased the scientific potential of the survey while still achieving sufficiently high SNRs. However, we also note that for surveys that have less extended sources or require very high SNRs, it is necessary to be more conservative in the MSA design.

## 4. Analysis

### 4.1. Redshifts and Stellar Population Modeling

We derive redshifts and stellar population properties for all quiescent targets by fitting the 1D spectra for the quiescent targets in addition to their UltraVISTA DR3 photometry

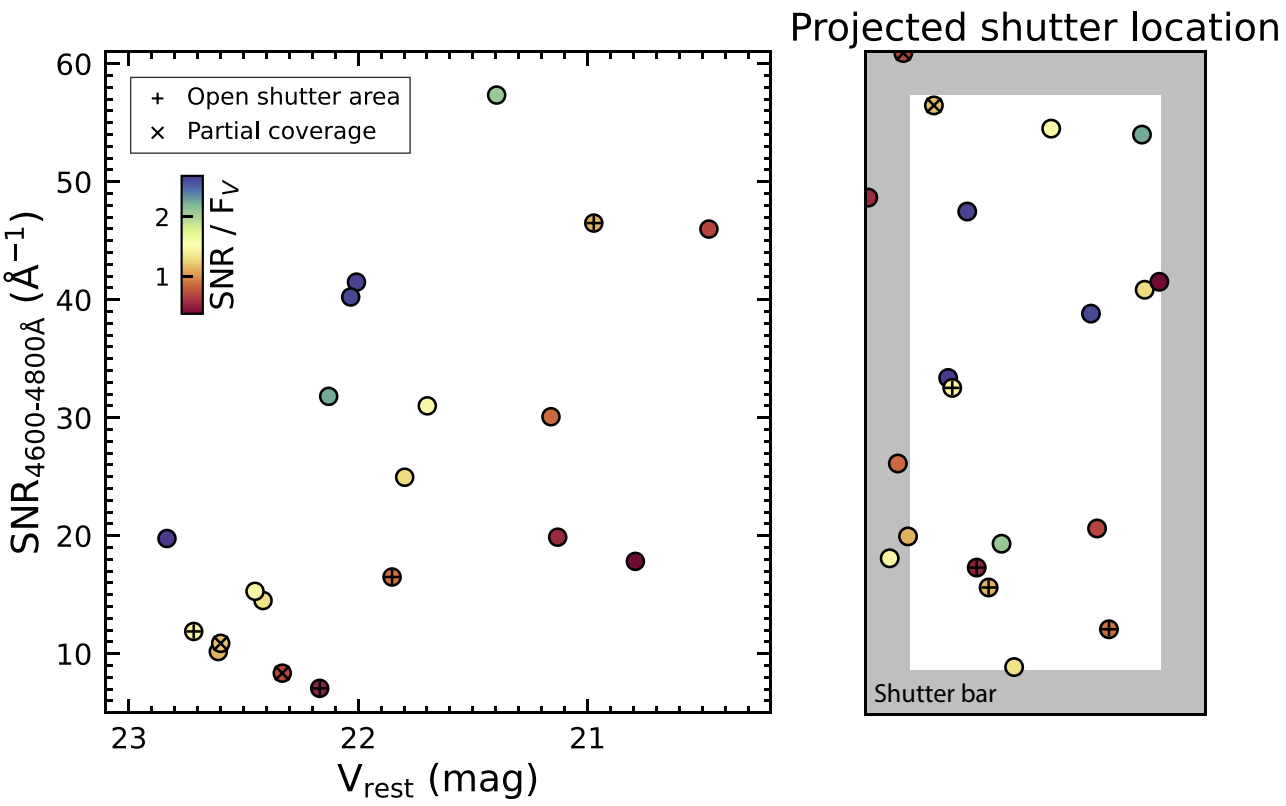


**Figure 5.** Median spectral SNR between rest-frame 4600–4800 Å against rest-frame *V*-band magnitude (left panel) and projected position on the shutter (right panel) for all quiescent targets. We color the symbols in both panels by the ratio of the SNR to rest-frame *V*-band flux. Sources that were observed in an area of the MSA that is affected by failed open shutters are indicated with a plus, and crosses represent sources that were not covered by all four nod/dither configurations. The gray area in the right panel shows the area of the shutter that is covered by part of the bar separating two shutters.

(Muzzin et al. 2013b) using the `Prospector` code (Leja et al. 2019b; Johnson et al. 2021). `Prospector` uses the Flexible Stellar Population Synthesis (`FSPS`; Conroy et al. 2009; Conroy & Gunn 2010) library, the MILES spectral library (Falcón-Barroso et al. 2011), and the MIST isochrones (Choi et al. 2016; Dotter 2016) to construct stellar population models. We used the `dynesty` dynamic nested sampling package (Speagle 2020) to sample the posterior distributions. We do not include the option in `Prospector` that fits for nebular emission lines in the spectrum, as the models used to fit for these emission lines are often not flexible enough to capture the observed line ratios due to the influence of, e.g., AGN, abundance ratios, or radiative transfer through dust. Instead, we masked out the spectrum within 50 Å of the [O II] $\lambda\lambda$3727, 3730 doublet and within 100 Å of the [O III] $\lambda\lambda$4960, 5000, [N II] $\lambda\lambda$6550, 6585, and [S II] $\lambda\lambda$6718, 6733 doublets. For galaxies with strong emission lines (127700, 128451, 130040, and 130647), we also correct the photometry for the contribution of emission lines before fitting. We also found that the deep Na D absorption feature biased the best-fit metallicity in some galaxies in our sample. We thus also mask out the spectrum within 50 Å of this feature. We describe the free parameters and priors that we used in our modeling below and summarize them in Table 2.

#### 4.1.1. SFH Models

We fit two models with different nonparametric SFHs to our data. The first SFH is the fixed-bin model described by Leja et al. (2019a). In this SFH, there are $N$ user-defined fixed time bins, all of which have a constant SFR that is varied in the fit. In our model, we used nine time bins, where the first two bins have lookback times of 0–30 Myr and 30–100 Myr and the last bin covers $0.85t_{\rm univ}$–$t_{\rm univ}$ at the redshift of the galaxy. The remaining six bins are spaced evenly in log-lookback time. The second SFH we fit is the poststarburst (PSB) model described by Suess et al. (2022a). This SFH model allows for more flexibility in the SFH, enabling it to capture short, recent bursts of star formation and rapid quenching. This is achieved by fitting an SFH with nine time bins, where the four oldest ($t > 0.6t_{\rm univ}$) bins have fixed bin edges, while the bin edges of the five youngest bins are varied in the fit. The four fixed bins have variable SFRs, whereas the five bins with flexible edges all form an equal amount of stellar mass. To capture low levels of star formation after the burst, the last bin has both a variable SFR and a variable bin edge.

For both SFH models, the SFR in each bin is determined by fitting the log of the ratio of the SFR in adjacent bins ($\log {\rm SFR}_{\rm ratio}$) using a Student $t$ prior. Following Suess et al. (2022b), we used predicted SFHs for quiescent galaxies from the UniverseMachine public data (Behroozi et al. 2019) to set physically motivated priors. To this end, we first found the UniverseMachine-predicted SFH for quiescent galaxies at the redshift of the galaxy to be fit, for a stellar mass of $\log M_*/M_\odot = 10.8$, corresponding to the UniverseMachine mass bin closest to the estimated stellar masses of galaxies in our sample. We then calculated the $\log {\rm SFR}_{\rm ratio}$ that would produce this SFH and used these values to set a Student $t$ prior with a width of 0.3 dex and a degree of freedom of 1.

**Table 2**
Parameters and Priors Used in the Prospector Fits

| | Parameter | Description | Prior |
|---|---|---|---|
| Global | $\log(M_*/M_\odot)$ | Total stellar mass formed | Uniform: min = 9.5, max = 12.5 |
| | $\log(Z_*/Z_\odot)$ | Stellar metallicity | Uniform: min = –1.4, max = 0.19 |
| | $\sigma$ | Stellar velocity dispersion | Uniform: min = 5, max = 600 km s$^{-1}$ |
| | $z$ | Redshift | Gaussian: $\mu$ = estimated $z_{spec}$, $\sigma = 0.05$ |
| Dust | $\hat{\tau}_{\lambda,2}$ | Diffuse dust optical depth | Uniform: min = 0.0, max = 2.5 mag |
| | $\hat{\tau}_{\lambda,1}$ | Birth cloud dust optical depth | Fixed to $\hat{\tau}_{\lambda,2}$ |
| | $n$ | Slope of Kriek & Conroy dust law | Uniform: min = −1.0, max = 0.4 |
| SFH | log $SFR_{ratio}$ | Ratio of SFR in adjacent bins | Student $t$ (8-vector): $\tau = 0.3$, $\nu = 1$ |
| SFH: PSB | log $SFR_{ratio,young}$ | Ratio of SFR in youngest bin to the last flex bin | Student $t$: $\tau = 0.3$, $\nu = 1$ |
| | log $SFR_{ratio,old}$ | Ratio of SFR in old bins to the first flex bin | Student $t$ (4-vector): $\tau = 0.3$, $\nu = 1$ |
| | log $SFR_{ratio}$ | Ratio of SFR in adjacent flex bins | Student $t$ (4-vector): $\tau = 0.3$, $\nu = 1$ |
| | $t_{last}$ | Width of youngest bin | Uniform: min = 0.01 Gyr, max = 0.3 $t_{univ}$ |
| Noise | $j_{spec}$ | Spectroscopic jitter term | Uniform: min = 1, max = 5 |
| | $f_{out}$ | Fraction of pixels in spectrum that are outliers | Uniform: min = 0.0, max = 0.5 |
| | $s_{out}$ | Inflation of the nominal noise for outlier pixels | Fixed to 50 |

**Notes.** The Student $t$ priors for the SFHs are centered at the UniverseMachine SFH predictions for a quiescent galaxy of similar mass and redshift, as described in the text.

For the fixed-bin SFH model, we fit the spectroscopic redshift of the galaxy using a Gaussian prior. We estimated the redshift of each galaxy by hand first and set this as the mean of the prior and the width to 0.05. The best-fit spectroscopic redshift of the fixed-bin model is then used as a fixed parameter in the PSB model. All other parameters in the fit are set up identically for the two models.

After fitting both SFH models, we determined for each galaxy which model best fits the data based on the lowest reduced $\chi^2$ statistic. The difference in the $\chi^2$ value between the two best-fit models ranges between ∼1% and 15% for the galaxies in our sample. We note that for galaxies with a very small difference between the two residuals, the best-fit SFHs and stellar population parameters of the two models are nearly identical.

#### 4.1.2. General Model Setup

We assumed the Chabrier (2003) IMF and added nebular continuum and dust emission using the standard Prospector parameters. In addition to the SFH shape, we also fit for the total stellar mass formed, metallicity, velocity dispersion, and dust attenuation. We set a flat prior on $\log M_*/M_\odot$ between 9.5 and 12.5 and let $\log Z/Z_\odot$ vary between −1.4 and 0.19, corresponding to the metallicity limits of the MILES spectral library (Falcón-Barroso et al. 2011). The velocity dispersion was varied between 5 and 600 km s$^{-1}$. The prior range for the velocity dispersion was chosen to be this extended in order to correct for uncertainties in the effective spectral resolution of NIRSpec/MSA, as we describe in more detail below.

We use the Kriek & Conroy (2013) dust law, in which the UV dust bump and dust slope are correlated. For the dust model, we set the optical depth and dust index as free parameters. We set a uniform prior on the dust index between −1 and 0.4 (Noll et al. 2009). For the diffuse dust optical depth, we used a flat prior from 0.0 to 2.5 mag and fixed the birth cloud dust optical depth such that young stars are attenuated twice as much as old stars (Wild et al. 2020).

#### 4.1.3. Noise Modeling and Calibration

To ensure that bad pixels and calibration issues did not heavily affect our fits, we fit for noise and calibration parameters. We included the Prospector pixel outlier model that inflates the uncertainties of a fraction $f_{outlier}$ of pixels by a factor $s_{outlier}$. We set a uniform prior on $f_{outlier}$ between 0.0 and 0.5 and fix $s_{outlier}$ to 50. Next, we fit for an increase of the noise of the spectrum by including the noise model described in Johnson et al. (2021), with a free spectroscopic jitter term that we varied between 1 and 5. Lastly, to account for poor calibration of the spectra, we include Prospector's polynomial spectral energy distribution (SED) model, which optimizes out a polynomial in the model spectrum. We use a 12th-order polynomial and find that the average scale of the polynomial correction is ∼5%–10%.

#### 4.1.4. Line-spread Function

To include the wavelength-dependent spectral resolution of NIRSpec in the fit, we broadened the model spectra by the line-spread function (LSF) calculated from the instrumental resolution curve provided in JWST User Documentation (JDox).[20] However, these resolution curves are prelaunch estimates for a uniformly illuminated slit, and recent results from, for example, de Graaff et al. (2024a), Nanayakkara et al. (2024), and Nidever et al. (2024) indicate that the true spectral resolution is significantly higher.

We model the true spectral resolution in the final rectified 2D frames for our sources based on their morphology and slit placement and find that the true resolution is a factor of ∼1.22–1.38 higher than the reported resolution (see Appendix A). This factor is independent of wavelength. In our modeling, we thus multiply the JDox resolution curve by the scaling factor we find for each galaxy. For galaxies for which no morphological measurements are available (6 out of 20 quiescent targets), we cannot model the exact LSF and instead assume a conservative factor of 1.2, corresponding to our modeled LSF of a uniformly illuminated slit.

We show the resulting best-fit model to the spectra and photometry for two representative quiescent galaxies in Figure 4. The spectra of all quiescent galaxies in the sample

[20] https://jwst-docs.stsci.edu/jwst-near-infrared-spectrograph/nirspec-instrumentation/nirspec-dispersers-and-filters#gsc.tab=0

(20 images) are available as a figure set, and we report the best-fit stellar population parameters in Table 1. The stellar masses we report are the surviving stellar masses, converted from the total stellar mass formed using the surviving mass fraction obtained in the Prospector fit.

For the star-forming galaxy targets, we derive spectroscopic redshifts by fitting Gaussians to the observed emission lines (see Appendix C). Multiple emission lines were detected for most filler galaxies, yielding robust spectroscopic redshifts for 46 out of 53 star-forming filler galaxies. For a few of the higher-redshift galaxies, only one emission feature was observed ([O II]). Nonetheless, due to the consistency between the spectroscopic and photometric redshift, we were confident about the line identification. For seven star-forming filler galaxies, no spectroscopic features were detected; these galaxies were not included in Appendix C and are omitted from the rest of this study. Though the redshifts for all star-forming galaxies have been derived from emission lines, we note that we detect continuum emission and absorption lines for many star-forming galaxies as well.

### 4.2. Evaluation of Best-fit Prospector Models

For all galaxies, the fit to the spectrum and photometry looks reasonable (see Figure 4). However, for some spectral regions, the models do not properly capture the spectrum due to the fact that the resolution of the MILES stellar library varies with wavelength; the resolution is high between ∼3750 and 7200 Å, but outside this range, the resolution is lower than the spectral resolution of our data. For targets with $z \gtrsim 2$, this affects the fits to the spectra at the blue end, where the models follow the overall shape of the observed spectra, but cannot capture details. At the upper wavelength limit, the low-resolution models affect galaxies in our sample with redshifts below $z \sim 1.5$. The spectra of these sources cover the rest-frame spectral region of $\lambda \gtrsim 6200$ Å where TiO and CN absorption bands are present. These absorption bands are characteristic of evolved carbon- and oxygen-rich stars (e.g., Lu et al. 2024) and are generally only visible for evolved stellar populations where young, blue stars do not dominate over this population (e.g., Allard et al. 2000; Almeida et al. 2012). Because of the low spectral resolution of the models, all galaxies in our sample with TiO absorption bands in the spectra have best-fit models that fit this spectral region poorly, both in overall spectral shape and in specific absorption features.

Constraining spectral models of distant galaxies outside the 3750–7200 Å wavelength range was very challenging in the pre-JWST era, since high-resolution ground-based observations have strong telluric absorption bands at these wavelengths. The spectra we present in this work show that JWST observations will provide the medium-resolution spectra needed to calibrate models blueward and redward of the current spectral coverage. Furthermore, these spectra can also be used to improve models for the influence of evolved stars in stellar populations with ages around ∼1 Gyr (e.g., Maraston 2005; Kriek et al. 2010; Zibetti et al. 2013; Lu et al. 2024).

We also note that for some galaxies, strong absorption lines (e.g., Mg I and Na I in galaxy 129149) are not captured by the best-fit model. One possible explanation for this discrepancy between the observed and model spectra is the fact that we fit the spectrum and photometry simultaneously. Currently, photometric data need to be included in the modeling in order to fit for inaccurate calibration of the spectra. However, by including photometry, there is less flexibility for the model to accurately fit the observed spectrum. A second explanation for the inaccurate fit of specific absorption lines like Mg I and Na I is the fact that Prospector only uses the solar chemical abundance pattern in its models. However, observations have shown that quiescent galaxies at high redshifts have nonsolar abundances (e.g., Choi et al. 2014; Maiolino & Mannucci 2019; Beverage et al. 2024a), leading to different relative depths of absorption lines in a spectrum. To properly constrain all absorption lines in the spectra, Beverage et al. (2024b) fit the abundance of individual elements in the galaxies. We refer to that paper for more details on the differences between the Prospector fits presented in this work and the results from chemical abundance modeling.

Another explanation for why Prospector fails to reproduce the very deep Na I D $\lambda\lambda$5891, 5897 Å absorption feature in some galaxies (e.g., 129133) is the fact that this line is also a tracer of neutral gas in the interstellar medium (ISM) as well as AGN outflows. Although a detailed analysis of the contributions of the ISM and outflows is beyond the scope of this research, we note that the contribution of neutral gas could be used to explain the excess Na I D absorption in distant quiescent galaxies (e.g., Jafariyazani et al. 2020; Belli et al. 2024; Davies et al. 2024).

Lastly, it is possible that for some galaxies, none of the stellar spectral templates used by Prospector describe the observed spectrum well, for example, due to poor modeling of the influence of evolved stars, chemical abundances, or AGN. Indeed, for galaxies for which we find a high (>3) best-fit spectroscopic jitter term (targets 128452 and 127154), it is likely that the templates do not match the observed data, resulting in a best-fit spectrum that does not fit the data well.

### 4.3. Sample Characteristics

Our quiescent galaxy candidate targets were selected to be at $z > 1.1$, are relatively bright, and fall in the quiescent box of the *UVJ* diagram. However, our selection criteria were only based on photometric information, leading to uncertainties in the redshifts and resulting rest-frame $U - V$ and $V - J$ colors. In this section, we present the sample characteristics we find when we include the spectroscopic information.

In Figure 6, we show the quiescent and star-forming targets in magnitude–redshift space relative to the parent distribution from the full UltraVISTA catalog. We only show the 46 out of 53 filler galaxies for which we could measure a spectroscopic redshift. This figure shows that nearly all quiescent targets are brighter than $H < 22.6$; our criteria to ensure that our spectra are sufficiently deep to achieve our science goals. Only one quiescent galaxy in our sample is fainter; this galaxy was initially added as a filler target when creating the MSA mask, but since the observed spectrum has a high enough SNR, we now include it in our quiescent galaxy sample (see Section 2.1). Since we prioritized bright star-forming galaxies when selecting filler targets, the majority of the star-forming targets are at the bright end of the parent distribution, and only ∼one-fifth of the star-forming galaxies are relatively faint compared to the complete population. We note that the magnitude–redshift diagram for the parent catalog is based on photometric redshifts only, which introduces (systematic) uncertainties on the background distribution.

The histogram in Figure 6 shows that the redshifts of the quiescent and star-forming targets in our sample are not

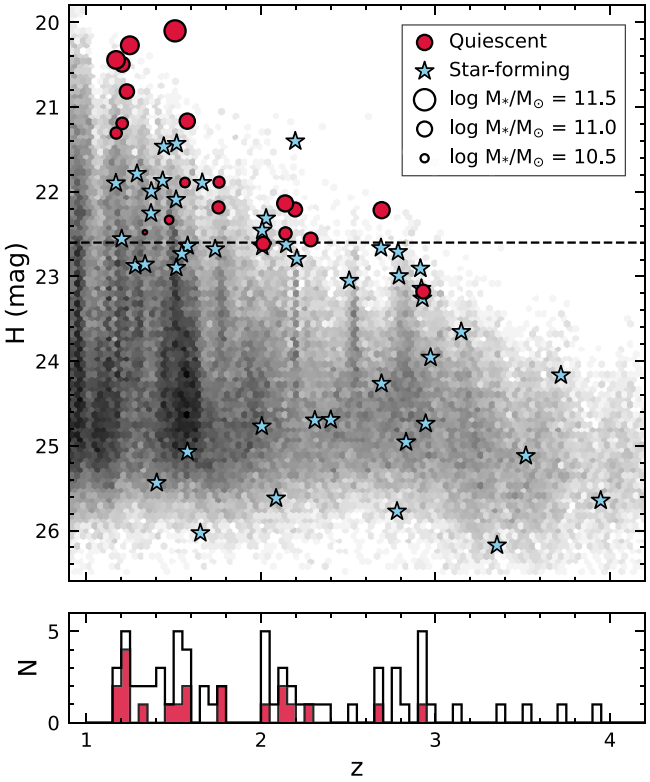


**Figure 6.** Top panel: *H*-band magnitude against redshift for all quiescent targets (red circles) and the filler targets for which we measured a spectroscopic redshift (blue stars). The symbol sizes of the quiescent targets are scaled by their `Prospector` best-fit stellar mass. The dashed line at $H = 22.6$ shows the magnitude limit we initially used to select our quiescent galaxy targets. One of our quiescent targets is fainter than this limit and was not prioritized when designing the MSA configuration. In the background, we show the parent UltraVISTA DR3 catalog from which our sample was drawn. Bottom panel: redshift distribution of all targets for which a spectroscopic redshift was measured (white shading). The red shaded histogram shows the redshift distribution of only the quiescent targets.

significantly clustered, except for a slight peak at $z \sim 1.2$. This peak may suggest that there could be a potential overdensity at this redshift, but, at face value, most of the galaxies in our sample do not appear to be part of an overdensity. This observation may be somewhat surprising, as we selected our pointing for the extraordinarily large number of quiescent galaxies we could observe within one MSA configuration. A detailed investigation into potential overdensities in our sample is beyond the scope of this paper.

In Figure 7, we show the rest-frame $U - V$ versus $V - J$ colors of all quiescent and star-forming targets, separated into three redshift bins. The *UVJ* colors were calculated from the photometry using `eazy` (Brammer et al. 2008), with the redshift set to the spectroscopic redshift. The top-left boxes in each panel indicate the region we used to select the quiescent targets (red symbols; Muzzin et al. 2013b), while star-forming targets lie outside of this box. For the initial selection of our quiescent targets, we used *UVJ* colors based on the photometric redshift. Three of our quiescent targets (IDs 127941, 128041, and 130725) scattered out of the box when using the spectroscopic redshift. However, since these galaxies lie very close to the selection box, they may still be recently quenched or PSB galaxies with quiescent stellar populations (e.g., Belli et al. 2019; Suess et al. 2021; Park et al. 2023). We will investigate the star formation properties of these galaxies in more detail in the next section.

The quiescent galaxy sample spans the full quiescent parent distribution in *UVJ* space, indicating that our sample is representative of the full distant quiescent galaxy population. Specifically, in the low-redshift bin, our sample contains old and red quiescent galaxies, while at higher redshifts, the quiescent galaxy sample shifts toward bluer colors. This is consistent with the younger ages we find for the bluer galaxies, as indicated by the colors of the symbols. This shift to younger ages and bluer galaxies is expected, as the Universe is much younger at this redshift.

### 4.4. Star Formation Properties

We have selected our quiescent galaxy sample based on their location in *UVJ* space. However, this selection was only based on photometric colors and redshifts, and galaxies with incorrect photometric redshifts may have erroneously scattered into the quiescent region, or the other way around. In the previous section, we indeed showed that after including spectroscopic redshifts, the *UVJ* colors of some galaxies shifted outside of the quiescent galaxy selection box. In order to assess whether our galaxies are indeed quiescent, we derived the star formation properties of our quiescent sample using the detailed SFHs obtained from the `Prospector` fits described in Section 4.1.

In Figure 8, we show the best-fit SFHs for four example galaxies in the quiescent sample. These four SFHs illustrate the diversity of SFHs in our sample. Galaxies 129966 and 127108 are best fit by the fixed-bin SFH model and have SFHs with long star formation timescales and gradual quenching. In contrast, 130183 and 130647 both have SFHs that are better fit by the PSB model, with a gradually increasing amount of star formation ending in a short burst, after which most of the star formation is suppressed. In total, 4 out of 20 primary targets (indicated in Table 1) have an SFH best described by the bursty PSB model, while 16 galaxies have more gradual fixed-bin SFHs. From this variety of SFHs, we find that the star formation timescales of galaxies in our sample range between $\sim$1 and 4 Gyr. We show the SFHs for all quiescent targets in Appendix B.

To assess whether our quiescent targets truly have quiescent stellar populations, we obtain their current SFRs from the `Prospector` best-fit SFHs (see Table 1). In Figure 9, we show the SFRs against the stellar mass of our quiescent sample. We also plot the Leja et al. (2022) star-forming main sequence (SFMS) ridge model at $z \sim 1$, $z \sim 1.5$, and $z \sim 3$. To decrease the dynamic range of this figure, we show the $3\sigma$ upper limit for sources with $\log \mathrm{SFR} < -1$. All data points lie $>2\sigma_{\mathrm{SFMS}}$ below the SFMS at their respective redshifts, which shows that all primary targets indeed have quenched star formation.

In the previous section, we found that three primary targets (IDs 127941, 128041, and 130725) had shifted outside the quiescent selection box of the *UVJ* diagram after including spectroscopic information. However, this selection box was empirically selected (Muzzin et al. 2013b) and will not be a hard limit for quiescence. Indeed, all of the galaxies outside the selection box lie $>7\sigma_{\mathrm{SFMS}}$ below the star-forming sequence, meaning their SFRs are strongly suppressed, and we include these galaxies in our quiescent sample.

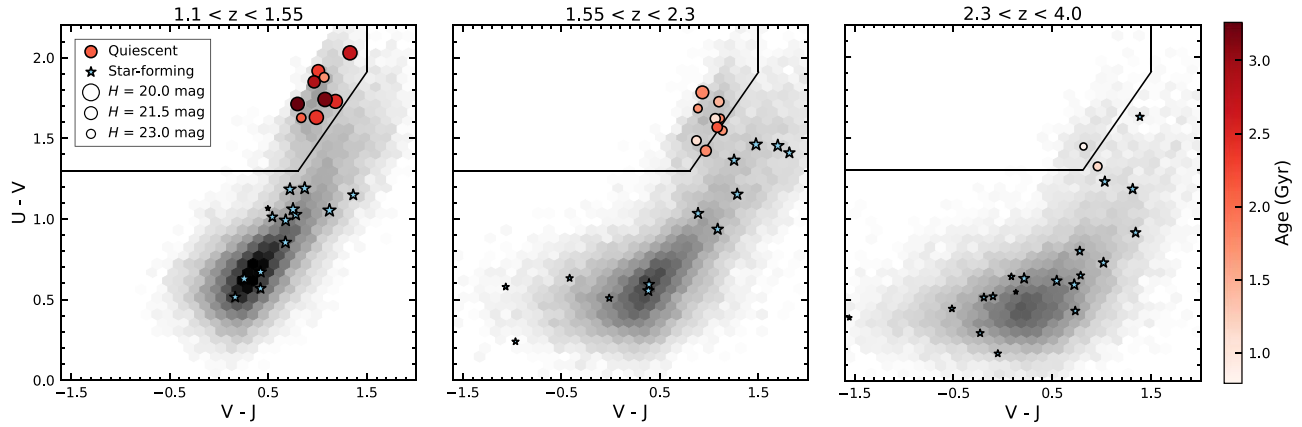


**Figure 7.** Rest-frame $U - V$ against $V - J$ colors for all galaxies observed in SUSPENSE, divided into three redshift intervals. Prior to the observations, candidate quiescent galaxies (red circles) were selected based on their rest-frame colors (obtained from photometric redshifts) using the indicated selection box (Muzzin et al. 2013b). However, when using spectroscopic redshifts, several candidate quiescent targets scattered just outside of this selection box. Nonetheless, all of these galaxies have confirmed quiescent stellar populations (see Section 4.4). We color the quiescent targets by their `Prospector` mass-weighted stellar age. The star-forming filler galaxies for which a spectroscopic redshift was measured are indicated by the blue stars. The size of each data point is scaled to the $H$-band magnitudes of the corresponding galaxy. In the background, we show the colors of galaxies in the parent UltraVISTA catalog for each redshift interval.

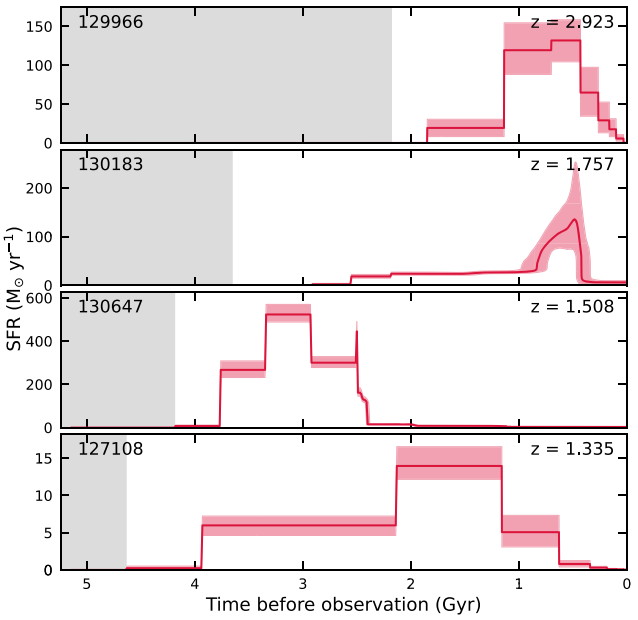


**Figure 8.** Four example best-fit SFHs for galaxies in the quiescent galaxy sample. The SFHs are ordered by decreasing redshift, as indicated in the top right of each panel. The red shaded areas represent the 16th–84th percentile confidence intervals of the SFHs. Targets 130183 and 130647 are best fit by a PSB SFH, while 129966 and 127108 have fixed-bin SFHs. The gray shaded area in each panel corresponds to ages that are older than the age of the Universe for the observed redshift.

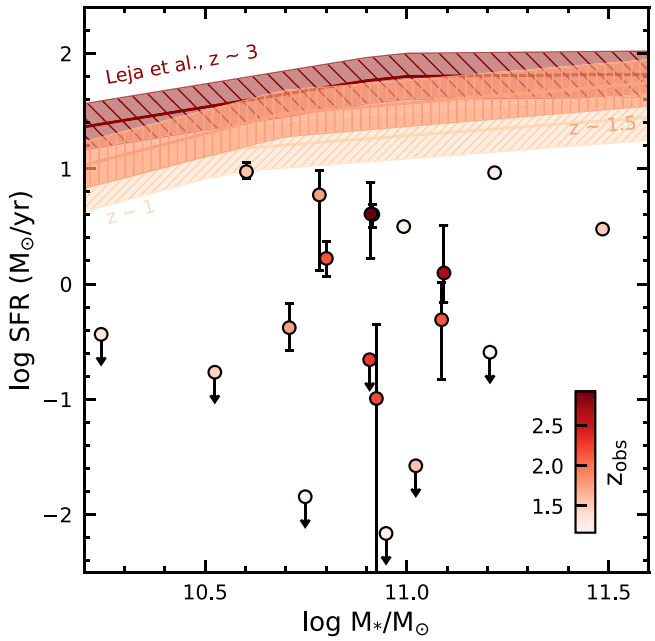


**Figure 9.** Stellar mass against SFR of the primary targets in our sample. For galaxies with $\log(\mathrm{SFR}/M_\odot\ \mathrm{yr}^{-1}) < -1$, we show a $3\sigma$ upper limit to decrease the dynamic range of the figure. The symbols are colored by the redshift at observation, and we show the Leja et al. (2022) SFMS for $z \sim 1$ (yellow shaded area), $z \sim 1.5$ (orange shaded area), and $z \sim 3$ (red shaded area). All candidate quiescent galaxies in our sample lie at least $2\sigma$ below the SFMS at their redshift.

### 4.5. Ages and Formation Times

We calculate the mass-weighted age of all primary galaxies from their SFHs (see Table 1). We show these mean stellar ages as a function of stellar mass in the left panel of Figure 10. The quiescent galaxies in our sample have ages of 0.8–3.3 Gyr and show a trend with observed redshift; the youngest galaxies in our sample were observed at the highest redshift. To illustrate how different spectral features are affected by the stellar age of a galaxy, we divide the sample into two age bins separated at a mass-weighted age of 1.8 Gyr. We create a median stack of the spectra of the galaxies in each age bin at a rest-frame wavelength range of 3600–6000 Å (right panel in Figure 10). Before stacking, we first normalized the spectra of each galaxy by its mean flux at 4600–4800 Å and resampled the spectra to a common wavelength grid.

From the stacked spectra, we can see clear differences in spectral features between the two age bins. For example, the 4000 Å break in the >1.75 Gyr stacked spectrum is more pronounced compared to the young age bin. Furthermore, the Balmer absorption lines of the young age bin are significantly deeper compared to continuum levels. This is clearest for the H$\delta$ and H$\gamma$ lines, which are sensitive to recently quenched star formation, while the difference in the depth of the H$\beta$ absorption line is less distinct between the two bins. This is

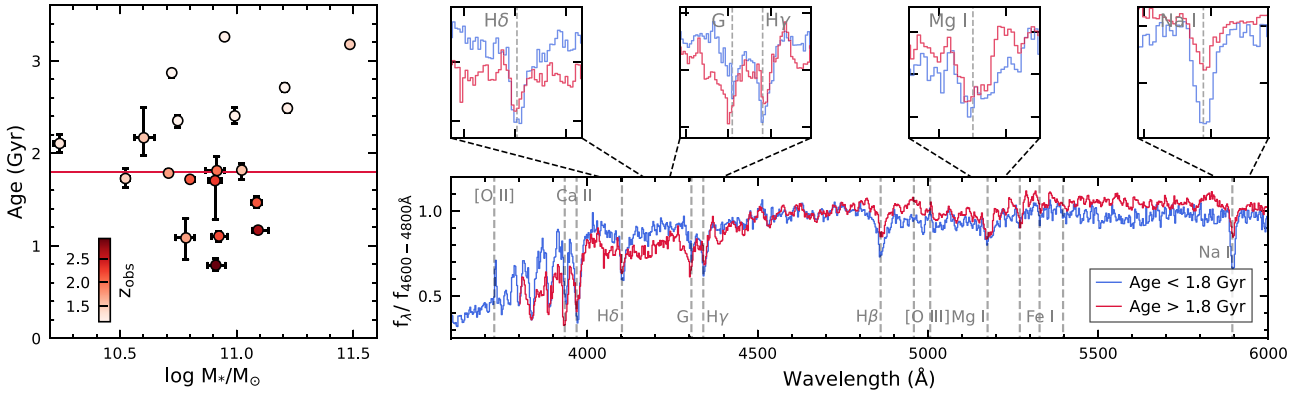


**Figure 10.** Left panel: mass-weighted age against stellar mass of all quiescent galaxies in our sample. The symbols are colored by the redshift of the target. The red line at 1.8 Gyr indicates the age we use to separate the sample into two age bins. Right panel: median-stacked spectrum of all galaxies in each age bin. The dashed vertical lines indicate Balmer, absorption, and emission features. The top-right panels zoom in on the spectral regions around H$\delta$, H$\gamma$, Mg I, and Na I to illustrate how these spectral features differ between the two age bins.

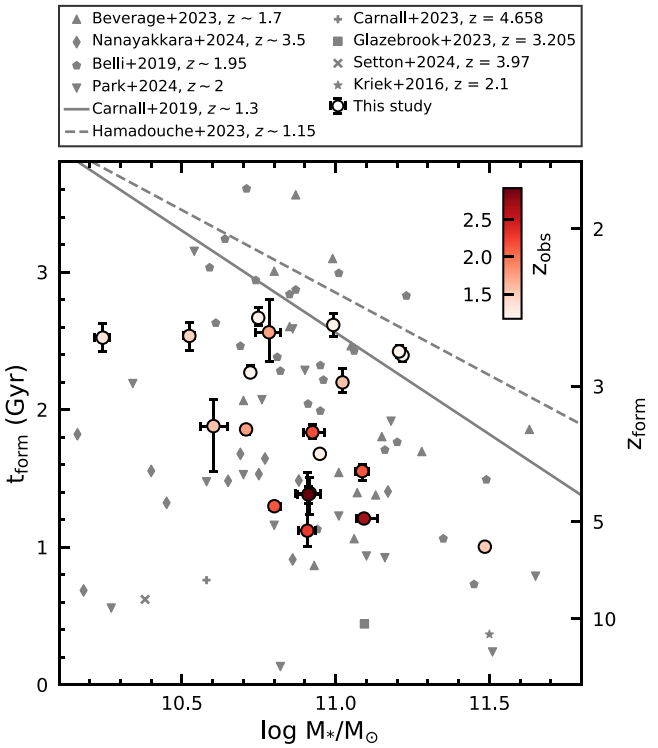


**Figure 11.** Age of the Universe where 50% of the stellar mass in the galaxy has formed ($t_{\rm form}$) as a function of stellar mass for all quiescent galaxies in our sample. The symbols are colored by the redshift at observation. We show the Nanayakkara et al. (2024) $z\sim3$ and 4 (gray diamonds), Beverage et al. (2024a) $z\sim1.7$ (gray triangles), Belli et al. (2019) $z\sim1.9$ (gray pentagons), and Park et al. (2024) $z\sim2$ (gray downward-pointing triangles) samples. Furthermore, we plot the mean relations from Carnall et al. (2019; solid gray line) and Hamadouche et al. (2023; dashed gray line) at $z\sim1.3$ and $z\sim1.15$, respectively. We also indicate four quiescent galaxies with early-onset star formation identified by Carnall et al. (2023a; gray plus), Glazebrook et al. (2023; gray square), Setton et al. (2024; gray cross), and Kriek et al. (2016; gray star).

likely because the youngest, most recently quenched galaxies still have some H$\beta$ emission, leading to a less deep absorption feature. The Mg I and Fe I metal absorption features, on the other hand, are significantly deeper for the old age bin due to the fact that lower-mass, cooler stars with more prominent metal absorption features start to dominate the spectrum at older ages. The Na I absorption line is instead deeper for the younger galaxies, likely due to the fact that this feature is also sensitive to neutral gas in the ISM, as well as AGN outflows. The distinct differences in the stacked spectra of the two age bins illustrate that several individual spectral features are strongly affected by the age of a galaxy and can be used to constrain detailed SFHs.

From the mass-weighted ages, we also calculate the formation times ($t_{\rm form}$) of the quiescent galaxies in our sample. Here $t_{\rm form}$ is defined as the age of the Universe at which 50% of the stellar mass in the galaxies has formed. In Figure 11, we show $t_{\rm form}$ as a function of stellar mass for our sample, with the symbols colored by the observed redshift. The galaxies in our sample have an average $t_{\rm form}$ of $\sim$1.0 and 2.7 Gyr, equivalent to a formation redshift between $z_{\rm form}\sim5.5$ and 2.5. We see no strong trend between average stellar formation time and stellar mass for our sample. For our massive galaxies, this is consistent with the findings of Carnall et al. (2019) and Gallazzi et al. (2014) at $z\sim1.1$ and $z\sim0.7$, respectively, who found that while there is a trend between mass and formation time at lower masses, this trend flattens out at $\log M_*/M_\odot \gtrsim 11$.

In Figure 11, we also show the spectroscopic samples by Nanayakkara et al. (2024) at $z_{\rm obs}\sim3$–4, Belli et al. (2019) at $z_{\rm obs}\sim1.95$, Park et al. (2024) at $z\sim2$, and Beverage et al. (2024a) at $z_{\rm obs}\sim1.7$. Furthermore, we show the mean relations from Carnall et al. (2019; $z_{\rm obs}\sim1.3$) and Hamadouche et al. (2023; $z_{\rm obs}\sim1.15$). The formation redshifts for most galaxies in these samples are consistent with those found for our sample at comparable redshifts.

Additionally, we show four high-redshift quiescent galaxies for which very early-onset star formation was identified from their spectra (Kriek et al. 2016; Carnall et al. 2023a; Glazebrook et al. 2023; Setton et al. 2024), with inferred formation redshifts of $z\sim8$. The Beverage et al. (2024a), Nanayakkara et al. (2024), and Park et al. (2024) samples also contain galaxies with formation redshifts $\gtrsim$6. These recent observations of early star formation in high-redshift quiescent targets suggest that the buildup of massive galaxies in the early Universe was much more rapid compared to the local Universe. Interestingly, while four galaxies in our sample were already quiescent by $z=3$, none of the quiescent galaxies in our sample have SFHs that are consistent with very early formation times.

Figure 11 shows a clear trend with redshift and mean formation time for our sample, with galaxies at lower redshift

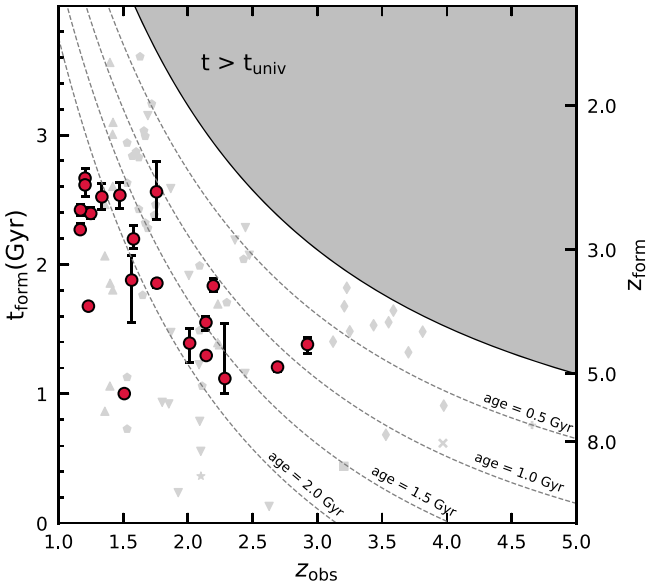


**Figure 12.** Age of the Universe where 50% of the stellar mass in the galaxy has formed ($t_{\rm form}$) as a function of the observed redshift ($z_{\rm obs}$) for all quiescent galaxies in our sample. The gray shaded area indicates the age of the Universe as a function of redshift, and the dashed gray lines indicate ages of 0.5–2.0 Gyr. We show different samples from the literature using the same symbols as in Figure 11.

generally forming later than the higher-redshift galaxies. In Figure 12, we show the formation time of our sample as a function of redshift and find that on average, the galaxies at $z_{\rm obs} > 1.75$ formed 50% of their stellar mass by $z \sim 4$, while for $z_{\rm obs} < 1.75$ galaxies, the mean formation redshift is $z \sim 3$. Furthermore, when we compare our sample with other samples at similar and higher redshifts, we see that our sample covers representative ages of the population across our redshift range, although we sample relatively more old galaxies compared to other studies.

### 4.6. Average SFHs

In Figure 13, we show the average SFHs of our galaxy sample, split into two redshift bins ($z_{\rm obs,\ lim} = 1.75$) with mean redshifts of $z_{\rm obs} = 1.3$ and $z_{\rm obs} = 2.2$. The middle panel of this figure shows the average mass buildup over time, calculated by taking the mean cumulative mass fraction as a function of time for all galaxies in the bin. The bottom panel of Figure 13 shows the summed SFRs as a function of the age of the Universe. Before summing the SFRs, all galaxies were normalized by their total stellar mass. We then smooth the summed SFRs of the redshift bins with a box kernel to reduce the noise from scatter in the individual galaxies' SFHs. Figure 13 shows that the summed star formation timescale is much shorter for galaxies at $z_{\rm obs} \sim 2.2$ compared to the $z_{\rm obs} \sim 1.3$ sample, consistent with the higher mean formation redshift we find for the galaxies at higher redshift. Furthermore, we also see that the onset of star formation is slightly later for the low-redshift bin.

Only one galaxy in the low-$z$ sample (130647) already had a significantly suppressed SFR at the redshifts at which the high-$z$ sample was observed (see Figure B1); all the other galaxies quench at later times. This galaxy forms its stars on a timescale that is comparable with galaxies in the high-$z$ bin, while all other galaxies in the low-$z$ bin form their stars over a longer period.

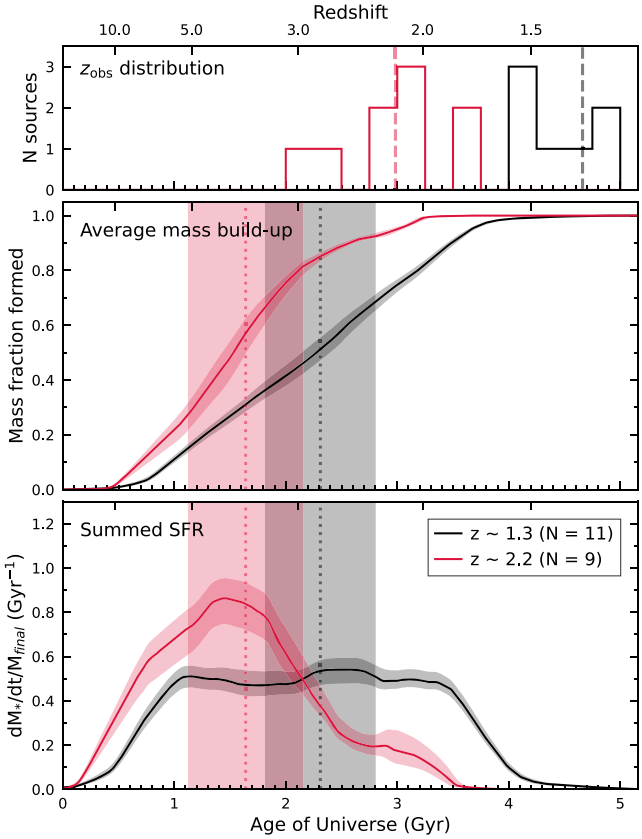


**Figure 13.** Top panel: distribution of the observed redshifts, separated into two redshift bins. The dashed lines indicate the mean redshift of each bin. Middle panel: the average SFH of all quiescent targets, separated into two redshift bins. Here the SFH corresponds to the total mass fraction formed as a function of the age of the Universe. Bottom panel: the summed SFR of all quiescent galaxies as a function of the age of the Universe, separated into two redshift bins. Before summing the SFRs of the galaxies, we first normalize them by their total stellar mass. The shaded regions around the mean SFHs indicate the error on the mean. In the middle and bottom panels, the dotted vertical lines indicate the average $t_{\rm form}$ of each redshift bin, with the vertical bands corresponding to the standard deviation of $t_{\rm form}$.

The galaxies within the two bins in Figure 13 have been observed at different redshifts and have different formation times, which will broaden the average star formation timescale of each bin. To account for this effect and compare the average intrinsic star formation timescale, we show an illustrative model for the typical SFHs for the two redshift bins, parameterized as a Gaussian in Figure 14. The FWHM of the Gaussian corresponds to the star formation timescale and is estimated from the median FWHM of the star formation timescales of the individual galaxies in the redshift bin. The mean of the typical SFH Gaussian is set to the median $t_{\rm form}$ of the redshift bin. It is important to note that this parameterization does not reflect the true shape of the SFHs but was chosen for its simplicity and should be taken as an illustration only. Nonetheless, there is a clear difference between the typical SFHs at $z_{\rm obs} \sim 1.3$ and $z_{\rm obs} \sim 2.2$, with higher-redshift quiescent galaxies forming more rapidly (FWHM = 1.0 Gyr) than their low-redshift counterparts (FWHM = 1.9 Gyr).

Interestingly, when we compare the inferred typical SFHs for the SUSPENSE sample with a sample of quiescent galaxies at similar redshifts ($z_{\rm obs} \sim 1.4$ and $z_{\rm obs} \sim 2.1$) from Beverage et al. (2024a), we see that our star formation timescales are a factor of $\sim$2 and $\sim$6 longer for the low- and high-redshift bins,

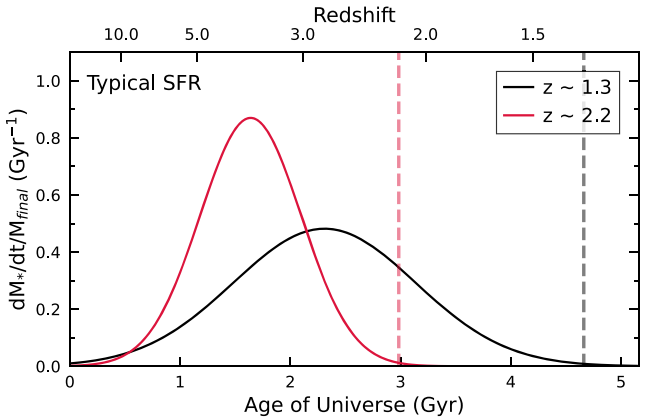


**Figure 14.** Illustrative "typical" SFH of quiescent galaxies at $z_{\rm obs} \sim 1.3$ and $z_{\rm obs} \sim 2.2$, assuming a simplistic Gaussian model. We take the mean of the Gaussian as the mean $t_{\rm form}$ of each sample, and the FWHM of the Gaussian corresponds to the median FWHM of the SFHs of the individual galaxies in each redshift bin. The median age of the Universe for the two redshift bins is indicated by the dashed lines. On average, quiescent galaxies at high redshift formed earlier and more rapidly than at low redshifts.

respectively. Similarly, Beverage et al. (2024b) measure detailed chemical abundances of the galaxies in our sample and find that while the mean stellar ages from this chemical abundance fitting are in good agreement with our findings, their star formation timescales are a factor of ∼6 shorter. This difference likely reflects the different methods to derive the star formation timescales; in Beverage et al. (2024a, 2024b), these are inferred from chemical abundances. These chemical abundance studies show that distant quiescent galaxies are carbon- and iron-deficient, implying that they quenched before significant enrichment by AGB stars and Type Ia supernovae, consistent with star formation scales of $\lesssim$200 Myr. In this study, on the other hand, we model the full SFH using a nonparametric model, which is likely biased to older, more extended SFHs by design (Leja et al. 2019a, 2019b; Carnall et al. 2024). We thus note that our timescales may be biased to be longer, though the trend with redshift that we find appears to be real. For a more detailed discussion of the comparison between the star formation timescales, we refer the reader to Beverage et al. (2024b).

## 5. Discussion

### 5.1. Implications for the Evolution of the Massive Quiescent Galaxy Population

In the previous section, we showed that the star formation timescales of massive quiescent galaxies become significantly shorter from $z_{\rm obs} \sim 1.3$ to $z_{\rm obs} \sim 2.2$. This indicates that the mass buildup of distant quiescent galaxies is much more rapid compared to later times. This result is consistent with the findings from Beverage et al. (2024a), who show that this trend extends from $z \sim 2.1$ up to $z \sim 0$. Furthermore, observations of quiescent galaxies out to $z \sim 5$ (e.g., Forrest et al. 2020b; Carnall et al. 2023b; Glazebrook et al. 2023; Setton et al. 2024) suggest that the evolution of the star formation timescale extends to even earlier times. In this section, we discuss the implications for the evolution of the quiescent galaxy population from these observations.

One explanation for the observed evolution in the star formation timescale across redshift is progenitor bias (van Dokkum & Franx 2001); between $z_{\rm obs} \sim 1.3$ and $z_{\rm obs} \sim 2.2$, the quiescent galaxy population grows in number as more star-forming galaxies are quenched. Thus, in our low-redshift bin, there are more galaxies that formed more gradually (i.e., longer star formation timescales) and entered the quiescent population at a later time.

A second explanation for the evolution of the SFHs is mergers, which change the properties of individual galaxies. In this scenario, major and minor mergers add new stellar populations to the galaxy, with SFHs that are different from those from the stars that are formed in situ. If the SFH of the accreted galaxy is more extended, or if the stars in that galaxy are younger, we would find that the SFH is broadened. The importance of minor mergers in the evolution of the quiescent galaxies has been supported by observations of the evolution in size and color gradients (e.g., Bezanson et al. 2009; Naab et al. 2009; van Dokkum et al. 2010; Suess et al. 2020, 2021; Miller et al. 2023). Furthermore, observations have shown that distant quiescent galaxies are surrounded by numerous small companions, which may merge into the central galaxy at later times (Newman et al. 2012; Suess et al. 2023).

If progenitor bias, rather than mergers and late-time star formation, is the main driver behind the observed evolution of the star formation timescale, this would imply that quiescent galaxies that formed rapidly in the early Universe should still exist as rare relics in the population at lower redshifts. Directly calculating the expected number of these remnant galaxies in our low-redshift sample is challenging due to the fact that we have observed only one pointing, selected for its exceptionally high number of distant quiescent galaxies. However, since all targets that we initially selected to be quiescent were indeed confirmed to be quiescent and had broadly consistent spectroscopic and photometric redshifts, we can infer that the success rate of photometrically identifying distant quiescent galaxies at $1 < z < 3$ is extremely high (100% for our survey).

Thus, we can compare the number densities of quiescent galaxies with $10.50 < \log(M_*/M_\odot) < 11.25$ at $z = 2.5$ and $z = 1.5$ from McLeod et al. (2021) and find that the number densities increase by a factor of ∼3.5. This implies that, if we assume no evolution of individual galaxies, 1 out of 3.5 quiescent galaxies at $z \sim 1.5$ was already quiescent at $z \sim 2.5$. Naively, we would thus expect to find that ∼3 out of 11 sources in our low-redshift bin are remnant galaxies. However, in our sample, only one galaxy (130647) in the $z_{\rm obs} \sim 1.3$ bin was already quiescent at $z \sim 2.5$. The reason that we find fewer remnant galaxies than expected could thus be easily explained by the late-time evolution of galaxies that quenched by $z \sim 2.5$ through late-time star formation or mergers. On the other hand, as our sample is small and the selection is based on magnitude, we should be cautious when interpreting these results, since it is possible that we have missed fainter, older remnant galaxies in our sample.

Thus, our observations suggest that population growth alone likely cannot explain the observed evolution of the star formation timescale at $z > 1$, and instead, mergers and late-time star formation should also contribute to this evolution. On the other hand, the short star formation timescales (200 Myr) and similar formation times that Beverage et al. (2024b) find for the galaxies in the $z_{\rm obs} \sim 1.3$ bin imply that all galaxies in our sample would have been quiescent by $z \sim 2.5$. This result is difficult to reconcile with the evolving number densities of quiescent galaxies between the low- and high-redshift bins. However, since the reported star formation timescales of

Beverage et al. (2024b) are based on sample averages, caution is needed to interpret these results. Thus, larger samples for which (resolved) chemical abundance and kinematic measurements and detailed SFHs are constrained are needed to solve this tension and will allow us to investigate the influence of minor and major mergers on the observed evolution in star formation timescales in more detail.

### 5.2. Implications for "Maximally Old" Distant Quiescent Galaxies

Several spectroscopic studies of distant quiescent galaxies have shown indications of massive galaxies that have already formed nearly all their stars by $z = 5$ (e.g., Kriek et al. 2016; Forrest et al. 2020b; Carnall et al. 2023b; Beverage et al. 2024a; Glazebrook et al. 2023; Setton et al. 2024). In our sample, the most extreme galaxy has an average formation redshift of $z \sim 5.5$ and formed nearly all its stars by $z \sim 3$. Thus, our galaxies are not as extreme as the ones found by the above studies.

The lack of maximally old galaxies in our sample could be explained in part by the fact that the observation redshift of our sample is lower compared to most of the studies mentioned above. If the evolution of the quiescent galaxy population is driven by progenitor bias, there would be relatively fewer extremely old galaxies at lower redshifts as newly quenched galaxies are added to the population. On the other hand, if merging is the main driver of the evolution of the quiescent population, galaxies that quenched early in the Universe would likely merge with lower-mass galaxies after they become quiescent. These mergers would then shift the SFH of this initial early quencher to a later formation time and more extended SFH. Thus, if mergers are dominant, it is unlikely that we detect galaxies with a formation redshift of $z > 10$ in our sample at $z \sim 3$.

Irrespective of the evolutionary scenario, we will thus, by construction, have fewer maximally old galaxies in our sample, as the low-redshift population, on average, quenched (and thus formed) at a later time compared to samples at higher redshifts. Furthermore, while previously detected maximally old galaxies are often extremely massive and/or bright, our sample is more representative of the complete quiescent galaxy population (see Figure 7), without a strong bias for extremely bright or massive galaxies. Compared to previous studies of maximally old galaxies, our galaxy sample thus presents a more complete overview of the quiescent galaxy population at its redshift, making the detection of maximally old galaxies less likely.

Furthermore, the low number densities of these "maximally old" sources make it unlikely that our sample includes a maximally old galaxy. Glazebrook et al. (2023) calculate a number density of $6 \times 10^{-7}$ Mpc$^{-3}$ for this type of galaxy, which corresponds to ∼0.05 maximally old galaxies per MSA pointing. With our single pointing, it is thus not surprising that our sample does not include such objects.

We also note that the methods for obtaining the stellar age differ between our study and other studies presenting maximally old galaxies, leading to uncertainties in comparing the mean formation times of these samples. First, the ages of the galaxies presented by Forrest et al. (2020b), Glazebrook et al. (2023), Nanayakkara et al. (2024), and Setton et al. (2024) were inferred from low-resolution spectra for which individual metal absorption features cannot be resolved. Without measurements of individual metal absorption features, it is difficult to break the age–metallicity degeneracy, leading to large uncertainties in the reported stellar ages for these galaxies. Furthermore, while the Kriek et al. (2016) and Beverage et al. (2024a) samples modeled the individual metal absorption features, the final age was modeled as a simple single or two-component age, rather than a full SFH. This simplification of the SFHs of these samples compared to the nonparametric SFHs used in this study makes comparison between the our study and these studies more challenging.

We note that our current study also suffers from modeling uncertainties, particularly as we model the photometric and spectroscopic data simultaneously. Interestingly, Beverage et al. (2024b) fit our spectra with `alf` (Conroy & van Dokkum 2012; Conroy et al. 2018) to constrain individual abundances and ages simultaneously while not taking photometry into account and find ages that are consistent with the ages inferred from `Prospector`, suggesting that different chemical abundance patterns and including photometry do not significantly bias the best-fit ages. However, we do note that our inferred SFHs could be biased to late-time star formation, as younger stellar populations will have more weight than the oldest stars in the galaxy, leading to more extended and younger SFHs.

## 6. Summary

In this paper, we present an overview and first results of the Cycle 1 JWST-SUSPENSE program. This ultradeep spectroscopic survey targeted 20 distant quiescent galaxy candidates at $z = 1$–3, as well as 53 star-forming galaxies at similar and higher redshifts. The observations were executed with the NIRSpec MSA using the G140M-F100LP dispersion-filter combination resulting in a rest-frame wavelength coverage of ∼3000–7000 Å at the targeted redshift. We use ∼five shutter slitlets and a two-shutter nod to observe the full extent of our primary targets and avoid self-subtraction. With 16 hr of on-source integration time, the SUSPENSE program has obtained the largest sample of quiescent galaxies with ultradeep (18 galaxies with continuum SNR $> 10$ Å$^{-1}$) medium-resolution spectra at $z > 1$ to date.

The spectra of all quiescent targets show clear Balmer and/or metal absorption features. Our quiescent galaxy sample is representative of the full quiescent galaxy population in our redshift range in *UVJ* space. We fit spectroscopic redshifts, stellar population parameters, and detailed SFHs for all quiescent targets in our sample using spectrophotometric fitting with `Prospector`. All galaxies in our sample are massive, with stellar masses ranging from $10^{10.24}$ to $10^{11.49}$ $M_\odot$. We used the best-fit SFHs to determine the SFRs and find that all 20 of our primary targets lie $>2\sigma$ below the SFMS at their redshift, indicating that they are indeed quiescent galaxies. Eleven of our targets show emission lines in their spectra (primarily [O II] and [N II] emission), likely originating from ionization due to an AGN or hot evolved stars. These emission lines will be the subject of a future study.

The mass-weighted ages of the galaxies in our sample range from 0.8 to 3.3 Gyr, with star formation timescales between ∼0.5 and 4 Gyr. Four galaxies in our sample were already quiescent by $z = 3$. On average, the high-redshift galaxies formed earlier than their low-redshift counterparts; 50% of the stellar mass of galaxies in the $z \sim 2.2$ bin formed at $z_{\rm form} \sim 4$, while for the $z \sim 1.3$ bin, the average formation redshift is $z_{\rm form} \sim 3$. This difference in formation redshift is consistent

with the typically shorter star formation timescales we find for galaxies at $z \sim 2.2$ compared to $z \sim 1.3$.

The observed evolution in SFHs can be explained by the growth of the quiescent galaxy population as the Universe ages; at lower redshifts, the addition of new galaxies with more extended SFHs alters the *average* SFH properties of the quiescent population. However, number density calculations show that mergers and/or late-time star formation likely also contribute to the observed evolution.

In future studies, we will expand upon this analysis by studying the (resolved) stellar, chemical, and kinematic properties of our quiescent targets. Thus, SUSPENSE presents a unique sample that will help us further unravel how these massive quiescent galaxies formed, when and why their star formation quenched, and how they evolved into the local quiescent population. Moreover, the spectra from the SUSPENSE program illustrate the power of JWST to obtain the deep, high-resolution spectroscopy needed to study distant, massive quiescent galaxies in great detail. Thus, JWST has marked a new era, in which ultradeep data will revolutionize our understanding of the formation and evolution of quiescent galaxies over cosmic time.

## Acknowledgments

This work is based on observations made with the NASA/ESA/CSA James Webb Space Telescope. The data were obtained from the Mikulski Archive for Space Telescopes at the Space Telescope Science Institute, which is operated by the Association of Universities for Research in Astronomy, Inc., under NASA contract NAS 5-03127 for JWST. These observations are associated with program JWST-GO-2110. Support for program JWST-GO-2110 was provided by NASA through a grant from the Space Telescope Science Institute, which is operated by the Association of Universities for Research in Astronomy, Inc., under NASA contract NAS 5-03127. M.K. acknowledges funding from the Dutch Research Council (NWO) through the award of the Vici grant VI.C.222.047 (project 2010007169). P.E.M.P. acknowledges the support from the Dutch Research Council (NWO) through the Veni grant VI.Veni.222.364.

*Facility:* JWST (NIRSpec). The JWST data presented in this article were obtained from the Mikulski Archive for Space Telescopes (MAST) at the Space Telescope Science Institute. The specific observations analyzed can be accessed via doi: 10.17909/6wjp-qb35.

*Software:* `Prospector` (Leja et al. 2019a; Johnson et al. 2021), `MSAEXP` (https://github.com/gbrammer/msaexp), `EAZY` (Brammer et al. 2008), `SExtractor` (Bertin & Arnouts 1996), `grizli` (Brammer 2023), `MSAFIT` (de Graaff et al. 2024a)

## Appendix A
## NIRSpec Resolution

The instrumental resolution for NIRSpec is provided for a uniformly illuminated slit in JDox.[21] However, since our quiescent sources are relatively compact, they will not uniformly illuminate the MSA slits, which will improve the actual instrumental resolution of our observed spectra (e.g., de Graaff et al. 2024a; Nanayakkara et al. 2024; Nidever et al. 2024).

[21] https://jwst-docs.stsci.edu/jwst-near-infrared-spectrograph/nirspec-instrumentation/nirspec-dispersers-and-filters#gsc.tab=0

For each galaxy, we derive the wavelength-dependent resolution in a rectified, combined spectrum, taking into account the source morphology and slit placement. Our method builds upon the work presented in de Graaff et al. (2024a), who model the LSF for an individual unrectified frame. Following de Graaff et al. (2024a), we use `MSAFIT` to create a 3D model cube of the source profile as a function of wavelength ($I(x, y, \lambda)$). We define this source profile as a Sérsic profile with the morphological parameters from Cutler et al. (2022) and sample the wavelength grid in intervals of $\Delta\lambda = 0.1$ $\mu$m, spanning the entire wavelength range of our filter/disperser combination. At each wavelength point, we insert an emission line with an intrinsic velocity dispersion of 0 and a total normalized intensity of 1. We set the location of the source in the slit as the source location given by the MSA reference file that is generated during the observations and use the shutters in which the source was observed. The model cube is then convolved with the point-spread function (PSF) and modeled onto the detector plane by `MSAFIT`.

The resulting model corresponds to a spectrum from a single, unrectified frame. Rectifying and combining the individual frames will further broaden the spectra. To obtain an estimate of the instrumental resolution in the final rectified, combined frames, we thus have to apply the same reduction steps to these modeled individual frames as we do for the real observed data. To this end, we input the model spectra (one for each nodding position in our observation setup) into the same modified pipeline we used to reduce our data, starting from Stage 2 of the JWST Calibration Pipeline (see Section 3). After processing the model spectra through Stages 2 and 3 of the reduction pipeline, we obtain a rectified, combined 2D spectrum with the same format as the observed 2D spectrum. From this model 2D spectrum, we extract the 1D spectrum and fit the inserted emission lines with single Gaussians. The FWHMs of these Gaussians give us the resolution as a function of wavelength.

In the left panel of Figure A1, we show the modeled LSF for source 127345 in the rectified frame in red, as well as the LSF calculated in `MSAFIT` for an individual unrectified frame in blue. We also show the LSF for a uniformly illuminated slit from JDox in black. As expected, the resolution of the modeled source is better than that of a uniformly illuminated slit, and after rectifying and combining the frames, the resolution decreases slightly. In the right panel of Figure A1, we show the resolution curves for the rectified spectra of all galaxies in our sample. The improvement in resolution for the galaxies in our sample is a factor of 1.22–1.38.

We caution that when deriving the LSF for an individual galaxy, it is important to sample the inserted emission lines at sufficiently small wavelength intervals. We find that our measured LSF is not a smooth curve for both the rectified and unrectified frames. The pattern we measure does not reflect a true discontinuity in the LSF but originates from the fact that the wavelength grid is undersampled for our filter/disperser combination, causing the inserted emission lines to not all be dispersed over the same pixel area. For a constant line intensity, this means that the measured width of the emission line in the spectrum will vary depending on what part of the pixels it is dispersed over. We note that this undersampling effect is especially clear in our modeling, as we model lines without intrinsic broadening; for broadened emission lines, the wavelength undersampling effect is less strong. To quantify how strong the variation in resolution due to undersampling is,

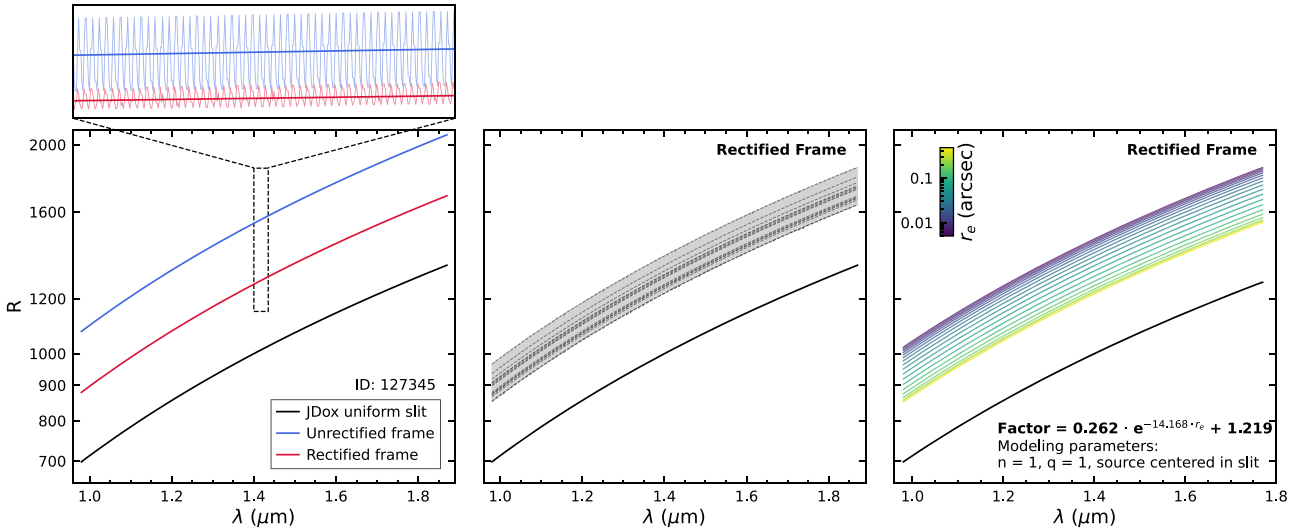


**Figure A1.** Left: the modeled resolution curve of NIRSpec for the F100LP/G140M filter/grating for source 127345 in the rectified frame (red line) and unrectified frame (blue line). The black solid line shows the dispersion curve for a uniformly illuminated slit from JDox. The inlay at the top shows sinusoidal patterns in the measured FWHMs due to wavelength undersampling. Middle: the range of resolutions for the rectified frame covered by the quiescent galaxies in our sample (gray area), with the mean curves of individual galaxies shown as dashed gray lines. The black solid line shows the dispersion curve for a uniformly illuminated slit from JDox. For the galaxies in our sample, the resolution is a factor of 1.22–1.38 higher than the reported resolution from JDox. Right: the resolutions in the rectified frame for sources with sizes ranging from $r_e = 0.''005$ (point source) to $r_e = 0.''48$ (uniformly illuminated slit) for a source that is centered in the slit, has a Sérsic index of 1, and $q = 1$. The black solid line shows the dispersion curve for a uniformly illuminated slit from JDox. To obtain the LSF for a source with a given $r_e$, we multiply the JDox resolution curve by the factor calculated using the formula in the bottom right of the plot.

we insert emission lines in an oversampled wavelength grid. We do this by creating 100 model cubes, each with emission lines at $\Delta\lambda = 100$ Å, but we shift the position of the emission lines by 1 Å for each model cube. We then measure the FWHMs of the emission lines for each of these models to obtain the LSF sampled at $\Delta\lambda = 1$ Å. We show the results of this test in the zoomed-in plot in Figure A1. This test shows that in the rectified frame, the variation from the median resolution due to undersampling is $R \sim 60$, while in the unrectified frame, the variation is $R \sim 235$. We obtain the final LSF for each galaxy from the average of the oversampled FWHMs from this test.

To understand how morphology and slit position affect the LSF, we additionally perform two tests. First, we assess the difference in resolution from source size by varying the half-light radius ($r_e$) from $0.''005$ (point source) to $0.''48$ (fully illuminated slit). We center the source in the slit, and use a Sérsic index of 1 and an axis ratio of 1. From this test, we find a difference in resolution of ∼18%, with a point source having the highest resolution and a uniformly illuminated slit having the lowest resolution. We note that the estimated resolution of the uniformly illuminated slit is still significantly higher (a factor of ∼1.2) than the resolution reported by JDox. We fit an exponential relation to the multiplication factors we find for our range of $r_e$ values and find that the multiplication factor depends on $r_e$ as

$$\text{Factor} = 0.262 \cdot e^{-14.168 \cdot r_e} + 1.219. \quad \text{(A1)}$$

Second, we test the effect of the source position in the slit by calculating the resolution of a source with a Sérsic index of 1, an axis ratio of 1, and an effective radius of $0.''05$ for different positions in the slit. We first test the effect of the placement along the dispersion direction and find that the maximum difference in resolution from moving it along the slit in this direction is 11%. We also note that in some cases the resolution of a source that is slightly off-center is somewhat higher than a completely centered source. This is likely due to undersampling effects. When we vary the source placement along the spatial direction, we find that the improvement in resolution from a source at the edge of the slit compared to a centered source is 3%.

While these tests are insightful to see the approximate effect of source morphology and slit placement on the resolution, we emphasize that the full source needs to be modeled in the `MSAFIT` software to obtain a reasonable estimate for the true resolution of the source. We also note that the modeling using `MSAFIT` is still subject to further calibration (for details, see de Graaff et al. 2024a) but is sufficiently accurate for the purposes of this work.

## Appendix B
## SFHs

In Section 4.1, we fit stellar population parameteres of the quiescent galaxies in the SUSPENSE program using Prospector. The resulting best-fit SFHs for all galaxies are presented in Figure B1.

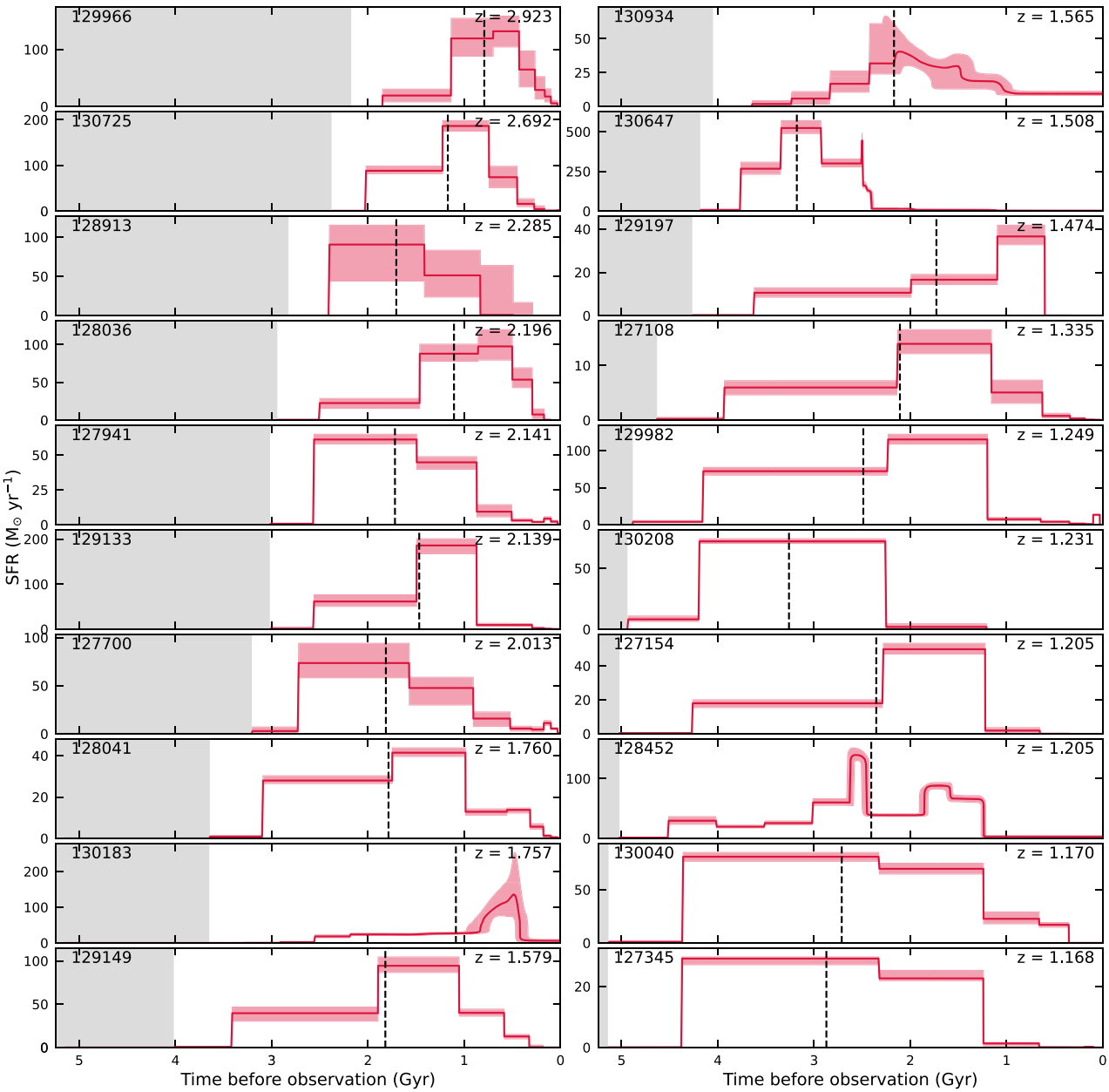


**Figure B1.** Best-fit SFHs for all galaxies in the quiescent sample. The SFHs are ordered by decreasing redshift, as indicated in the top right of each panel. The shaded areas represent the 16th–84th percentile confidence intervals of the SFHs. The black dashed vertical lines indicate the time where 50% of the galaxy's stellar mass was formed ($t_{50}$). The gray shaded area in each panel corresponds to ages that are older than the age of the Universe for the observed redshift.

## Appendix C
## Filler Galaxies

In Section 4.1, we fit the redshifts of all star-forming galaxies observed with the SUSPENSE program. We present these redshifts and other properties of this sample in Table C1.

**Table C1**
Overview of Confirmed Star-forming Filler Galaxy Sample

| ID | Coordinates | | $H$ | $z_{spec}$ | Rest-frame Colors | | $t_{exp}$ (hr) |
|---|---|---|---|---|---|---|---|
| | R.A. | Decl. | | | $U-V$ | $V-J$ | |
| 126887 | 10:01:58.27 | 2:25:44.3 | 25.1 | 1.579 | 0.63 | −0.42 | 4.9 |
| 127350 | 10:02:01.03 | 2:26:00.2 | 22.3 | 2.030 | 1.36 | 1.25 | 6.6 |
| 127491 | 10:01:57.73 | 2:26:13.9 | 21.9 | 1.169 | 0.63 | 0.26 | 13.1 |
| 127646 | 10:02:02.00 | 2:26:28.2 | 25.0 | 2.832 | 0.45 | −0.51 | 16.4 |
| 127680 | 10:01:59.64 | 2:26:25.1 | 22.7 | 1.738 | 0.94 | 1.09 | 16.4 |
| 127894 | 10:02:04.90 | 2:26:41.2 | 25.1 | 3.518 | 0.64 | 0.09 | 11.5 |
| 127900 | 10:01:57.88 | 2:26:39.4 | 22.6 | 1.202 | 0.67 | 0.42 | 13.1 |
| 128019 | 10:02:00.72 | 2:26:44.3 | 22.5 | 2.007 | 1.15 | 1.28 | 16.4 |
| 128029 | 10:02:05.44 | 2:26:44.4 | 22.8 | 2.206 | 0.56 | 0.38 | 16.4 |
| 128047 | 10:02:01.12 | 2:26:42.6 | 21.4 | 2.197 | 1.46 | 1.48 | 6.6 |
| 128080 | 10:02:00.32 | 2:26:48.2 | 23.0 | 2.791 | 0.59 | 0.72 | 8.2 |
| 128188 | 10:02:01.66 | 2:26:52.4 | 21.9 | 1.664 | 1.45 | 1.70 | 16.4 |
| 128344 | 10:01:59.05 | 2:27:02.7 | 22.3 | 1.370 | 1.03 | 0.78 | 16.4 |
| 128345 | 10:02:05.39 | 2:27:05.0 | 22.6 | 2.008 | 1.03 | 0.89 | 3.3 |
| 128422 | 10:01:59.92 | 2:27:05.7 | 22.0 | 1.372 | 1.19 | 0.87 | 8.2 |
| 128444 | 10:02:05.94 | 2:27:09.0 | 22.7 | 2.786 | 0.62 | 0.54 | 9.8 |
| 128561 | 10:02:09.67 | 2:27:17.8 | 23.3 | 2.925 | 0.73 | 1.02 | 16.4 |
| 128827 | 10:02:04.39 | 2:27:35.3 | 23.7 | 3.148 | 0.80 | 0.78 | 6.6 |
| 128948 | 10:02:08.83 | 2:27:43.7 | 24.8 | 2.005 | 0.51 | −0.01 | 9.8 |
| 129015 | 10:01:57.29 | 2:27:47.4 | 24.7 | 2.309 | 0.51 | −0.19 | 4.9 |
| 129024 | 10:02:08.43 | 2:27:45.5 | 22.9 | 1.280 | 0.51 | 0.17 | 16.4 |
| 129161 | 10:02:07.06 | 2:27:49.5 | 21.9 | 1.437 | 1.18 | 0.72 | 16.4 |
| 129264 | 10:01:58.60 | 2:28:01.0 | 26.0 | 1.653 | 0.24 | −0.96 | 4.9 |
| 129315 | 10:01:55.81 | 2:28:03.1 | 24.7 | 2.944 | 0.29 | −0.23 | 8.2 |
| 129363 | 10:02:07.84 | 2:28:03.7 | 22.9 | 1.336 | 1.15 | 1.36 | 6.6 |
| 129508 | 10:01:55.56 | 2:28:12.6 | 23.1 | 2.920 | 0.92 | 1.34 | 8.2 |
| 129654 | 10:02:03.19 | 2:28:22.2 | 23.1 | 2.506 | 1.23 | 1.03 | 4.9 |
| 129663 | 10:02:02.95 | 2:28:25.3 | 24.2 | 3.719 | 0.65 | 0.79 | 8.2 |
| 129689 | 10:01:55.20 | 2:28:26.5 | 25.6 | 2.087 | 0.58 | −1.06 | 4.9 |
| 129695 | 10:01:55.81 | 2:28:21.0 | 22.7 | 2.688 | 1.18 | 1.31 | 8.2 |
| 129776 | 10:01:55.76 | 2:28:31.9 | 24.0 | 2.972 | 0.43 | 0.73 | 9.8 |
| 129829 | 10:01:54.33 | 2:28:32.0 | 22.6 | 1.580 | 0.59 | 0.39 | 6.6 |
| 129992 | 10:01:56.00 | 2:28:35.7 | 21.5 | 1.443 | 1.06 | 0.75 | 16.4 |
| 130128 | 10:02:07.20 | 2:28:51.5 | 25.8 | 2.780 | 0.39 | −1.55 | 8.2 |
| 130180 | 10:02:04.82 | 2:28:54.6 | 25.6 | 3.947 | 0.17 | −0.05 | 9.8 |
| 130293 | 10:01:55.28 | 2:28:58.0 | 22.9 | 1.515 | 0.57 | 0.42 | 16.4 |
| 130320 | 10:02:04.20 | 2:28:59.5 | 22.7 | 1.547 | 1.01 | 0.54 | 3.3 |
| 130390 | 10:02:06.12 | 2:29:06.5 | 26.2 | 3.353 | 0.55 | 0.13 | 16.4 |
| 130547 | 10:01:58.17 | 2:29:15.9 | 24.7 | 2.400 | 0.52 | −0.10 | 9.8 |
| 130782 | 10:02:05.29 | 2:29:26.1 | 22.1 | 1.514 | 0.85 | 0.68 | 3.3 |
| 130874 | 10:02:04.54 | 2:29:28.9 | 21.8 | 1.290 | 0.99 | 0.68 | 9.8 |
| 130907 | 10:02:04.55 | 2:29:31.8 | 21.4 | 1.517 | 1.05 | 1.12 | 16.4 |
| 130998 | 10:02:03.05 | 2:29:43.3 | 25.4 | 1.403 | 1.07 | 0.50 | 9.8 |
| 131179 | 10:02:03.86 | 2:29:49.5 | 22.6 | 2.145 | 1.41 | 1.81 | 6.6 |
| 131143 | 10:02:03.06 | 2:29:46.8 | 22.9 | 2.914 | 0.63 | 0.22 | 9.8 |
| 131221 | 10:02:04.55 | 2:29:54.1 | 24.3 | 2.691 | 1.63 | 1.38 | 16.4 |

(This table is available in machine-readable form in the online article.)

## ORCID iDs

Martje Slob https://orcid.org/0000-0001-7540-1544
Mariska Kriek https://orcid.org/0000-0002-7613-9872
Aliza G. Beverage https://orcid.org/0000-0002-9861-4515
Katherine A. Suess https://orcid.org/0000-0002-1714-1905
Guillermo Barro https://orcid.org/0000-0001-6813-875X
Rachel Bezanson https://orcid.org/0000-0001-5063-8254
Gabriel Brammer https://orcid.org/0000-0003-2680-005X
Chloe M. Cheng https://orcid.org/0000-0003-2251-9164
Charlie Conroy https://orcid.org/0000-0002-1590-8551
Anna de Graaff https://orcid.org/0000-0002-2380-9801
Natascha M. Förster Schreiber https://orcid.org/0000-0003-4264-3381
Marijn Franx https://orcid.org/0000-0002-8871-3026
Brian Lorenz https://orcid.org/0000-0002-5337-5856
Pavel E. Mancera Piña https://orcid.org/0000-0001-5175-939X
Danilo Marchesini https://orcid.org/0000-0001-9002-3502
Adam Muzzin https://orcid.org/0000-0002-9330-9108
Andrew B. Newman https://orcid.org/0000-0001-7769-8660
Sedona H. Price https://orcid.org/0000-0002-0108-4176
Alice E. Shapley https://orcid.org/0000-0003-3509-4855
Mauro Stefanon https://orcid.org/0000-0001-7768-5309
Pieter van Dokkum https://orcid.org/0000-0002-8282-9888
Daniel R. Weisz https://orcid.org/0000-0002-6442-6030

## References

Allard, F., Hauschildt, P. H., & Schwenke, D. 2000, ApJ, 540, 1005
Almaini, O., Wild, V., Maltby, D. T., et al. 2017, MNRAS, 472, 1401
Almeida, J. S., Terlevich, R., Terlevich, E., Fernandes, R. C., & Morales-Luis, A. B. 2012, ApJ, 756, 163
Antwi-Danso, J., Papovich, C., Esdaile, J., et al. 2023, arXiv:2307.09590
Asplund, M., Grevesse, N., Sauval, A. J., & Scott, P. 2009, ARA&A, 47, 481
Behroozi, P., Wechsler, R. H., Hearin, A. P., & Conroy, C. 2019, MNRAS, 488, 3143
Belfiore, F., Maiolino, R., Maraston, C., et al. 2016, MNRAS, 461, 3111
Belli, S., Contursi, A., Genzel, R., et al. 2021, ApJL, 909, L11
Belli, S., Newman, A. B., & Ellis, R. S. 2017, ApJ, 834, 18
Belli, S., Newman, A. B., & Ellis, R. S. 2019, ApJ, 874, 17
Belli, S., Park, M., Davies, R. L., et al. 2024, Natur, 630, 54
Bertin, E., & Arnouts, S. 1996, A&AS, 117, 393
Beverage, A. G., Kriek, M., Suess, K. A., et al. 2024a, ApJ, 966, 234
Beverage, A. G., Slob, M., Kriek, M., et al. 2024b, arXiv:2407.02556
Bezanson, R., van Dokkum, P. G., Tal, T., et al. 2009, ApJ, 697, 1290
Bournaud, F., Jog, C. J., & Combes, F. 2007, A&A, 476, 1179
Brammer, G. 2023, grizli, 1.8.3, Zenodo, 10.5281/zenodo.7767790
Brammer, G. B., van Dokkum, P. G., & Coppi, P. 2008, ApJ, 686, 1503
Bushouse, H., Eisenhamer, J., Dencheva, N., et al. 2023, JWST Calibration Pipeline, 1.12.5, Zenodo, 10.5281/zenodo.1002297
Carnall, A. C., Cullen, F., McLure, R. J., et al. 2024, arXiv:2405.02242
Carnall, A. C., McLeod, D. J., McLure, R. J., et al. 2023b, MNRAS, 520, 3974
Carnall, A. C., McLure, R. J., Dunlop, J. S., et al. 2019, MNRAS, 490, 417
Carnall, A. C., McLure, R. J., Dunlop, J. S., et al. 2022, ApJ, 929, 131
Carnall, A. C., McLure, R. J., Dunlop, J. S., et al. 2023a, Natur, 619, 716
Carollo, C. M., Bschorr, T. J., Renzini, A., et al. 2013, ApJ, 773, 112
Casey, C. M., Kartaltepe, J. S., Drakos, N. E., et al. 2023, ApJ, 954, 31
Cecchi, R., Bolzonella, M., Cimatti, A., & Girelli, G. 2019, ApJL, 880, L14
Chabrier, G. 2003, PASP, 115, 763
Chang, Y.-Y., van der Wel, A., Rix, H.-W., et al. 2013, ApJ, 773, 149
Choi, J., Conroy, C., Moustakas, J., et al. 2014, ApJ, 792, 95
Choi, J., Dotter, A., Conroy, C., et al. 2016, ApJ, 823, 102
Cimatti, A., Daddi, E., Renzini, A., et al. 2004, Natur, 430, 184
Conroy, C., & Gunn, J. E. 2010, ApJ, 712, 833
Conroy, C., Gunn, J. E., & White, M. 2009, ApJ, 699, 486
Conroy, C., & van Dokkum, P. G. 2012, ApJ, 760, 71
Conroy, C., Villaume, A., van Dokkum, P. G., & Lind, K. 2018, ApJ, 854, 139
Cutler, S. E., Whitaker, K. E., Mowla, L. A., et al. 2022, ApJ, 925, 34
Daddi, E., Renzini, A., Pirzkal, N., et al. 2005, ApJ, 626, 680
Davies, R. L., Belli, S., Park, M., et al. 2024, MNRAS, 528, 4976
de Graaff, A., Rix, H.-W., Carniani, S., et al. 2024a, A&A, 684, A87
de Graaff, A., Setton, D. J., Brammer, G., et al. 2024b, arXiv:2404.05683
D'Eugenio, F., Perez-Gonzalez, P., Maiolino, R., et al. 2023, arXiv:2308.06317
Dotter, A. 2016, ApJS, 222, 8
Esdaile, J., Glazebrook, K., Labbé, I., et al. 2021, ApJL, 908, L35
Falcón-Barroso, J., Sánchez-Blázquez, P., Vazdekis, A., et al. 2011, A&A, 532, A95
Ferruit, P., Jakobsen, P., Giardino, G., et al. 2022, A&A, 661, A81
Forrest, B., Annunziatella, M., Wilson, G., et al. 2020a, ApJL, 890, L1
Forrest, B., Marsan, Z. C., Annunziatella, M., et al. 2020b, ApJ, 903, 47
Forrest, B., Wilson, G., Muzzin, A., et al. 2022, ApJ, 938, 109
Franx, M., Labbé, I., Rudnick, G., et al. 2003, ApJL, 587, L79
Gallazzi, A., Bell, E. F., Zibetti, S., Brinchmann, J., & Kelson, D. D. 2014, ApJ, 788, 72
Gargiulo, A., Bolzonella, M., Scodeggio, M., et al. 2017, A&A, 606, A113
Glazebrook, K., Nanayakkara, T., Schreiber, C., et al. 2024, Natur, 628, 277
Glazebrook, K., Schreiber, C., Labbé, I., et al. 2017, Natur, 544, 71
Gould, K. M. L., Brammer, G., Valentino, F., et al. 2023, AJ, 165, 248
Grogin, N. A., Kocevski, D. D., Faber, S. M., et al. 2011, ApJS, 197, 35
Gu, M., Greene, J. E., Newman, A. B., et al. 2022, ApJ, 932, 103
Hamadouche, M. L., Carnall, A. C., McLure, R. J., et al. 2022, MNRAS, 512, 1262
Hamadouche, M. L., Carnall, A. C., McLure, R. J., et al. 2023, MNRAS, 521, 5400
Hartley, A. I., Nelson, E. J., Suess, K. A., et al. 2023, MNRAS, 522, 3138
Horne, K. 1986, PASP, 98, 609
Jafariyazani, M., Newman, A. B., Mobasher, B., et al. 2020, ApJL, 897, L42
Ji, Z., & Giavalisco, M. 2022, ApJ, 935, 120
Johnson, B. D., Leja, J., Conroy, C., & Speagle, J. S. 2021, ApJS, 254, 22
Khochfar, S., & Silk, J. 2006, ApJL, 648, L21
Koekemoer, A. M., Faber, S. M., Ferguson, H. C., et al. 2011, ApJS, 197, 36
Kriek, M., Beverage, A. G., Price, S. H., et al. 2024, ApJ, 966, 36
Kriek, M., & Conroy, C. 2013, ApJL, 775, L16
Kriek, M., Conroy, C., van Dokkum, P. G., et al. 2016, Natur, 540, 248
Kriek, M., Labbé, I., Conroy, C., et al. 2010, ApJL, 722, L64
Kriek, M., Price, S. H., Conroy, C., et al. 2019, ApJL, 880, L31
Kriek, M., van Dokkum, P. G., Franx, M., et al. 2006, ApJL, 649, L71
Kroupa, P. 2001, MNRAS, 322, 231
Lagos, C. d., Stevens, A. R. H., Bower, R. G., et al. 2018, MNRAS, 473, 4956
Leja, J., Carnall, A. C., Johnson, B. D., Conroy, C., & Speagle, J. S. 2019a, ApJ, 876, 3
Leja, J., Johnson, B. D., Conroy, C., et al. 2019b, ApJ, 877, 140
Leja, J., Speagle, J. S., Ting, Y.-S., et al. 2022, ApJ, 936, 165
Lu, S., Daddi, E., Maraston, C., et al. 2024, arXiv:2403.07414
Maiolino, R., & Mannucci, F. 2019, A&ARv, 27, 3
Maraston, C. 2005, MNRAS, 362, 799
Marchesini, D., Brammer, G., Morishita, T., et al. 2023, ApJL, 942, L25
Maseda, M. V., van der Wel, A., Franx, M., et al. 2021, ApJ, 923, 18
McCracken, H. J., Milvang-Jensen, B., Dunlop, J., et al. 2012, A&A, 544, A156
McLeod, D. J., McLure, R. J., Dunlop, J. S., et al. 2021, MNRAS, 503, 4413
Mendel, J. T., Beifiori, A., Saglia, R. P., et al. 2020, ApJ, 899, 87
Miller, T. B., van Dokkum, P., & Mowla, L. 2023, ApJ, 945, 155
Momcheva, I. G., van Dokkum, P. G., van der Wel, A., et al. 2017, PASP, 129, 015004
Mowla, L., van Dokkum, P., Brammer, G., et al. 2019, ApJ, 880, 57
Muzzin, A., Marchesini, D., Stefanon, M., et al. 2013a, ApJ, 777, 18
Muzzin, A., Marchesini, D., Stefanon, M., et al. 2013b, ApJS, 206, 8
Naab, T., Johansson, P. H., & Ostriker, J. P. 2009, ApJL, 699, L178
Naab, T., Oser, L., Emsellem, E., et al. 2014, MNRAS, 444, 3357
Nanayakkara, T., Glazebrook, K., Jacobs, C., et al. 2024, NatSR, 14, 3724
Newman, A. B., Belli, S., Ellis, R. S., & Patel, S. G. 2018, ApJ, 862, 126
Newman, A. B., Ellis, R. S., Bundy, K., & Treu, T. 2012, ApJ, 746, 162
Nidever, D. L., Gilbert, K., Tollerud, E., et al. 2024, in IAU Symp. 377, Early Disk-Galaxy Formation from JWST to the Milky Way, ed. F. Tabatabaei, B. Barbuy, & Y.-S. Ting (Cambridge: Cambridge Univ. Press), 115
Noll, S., Pierini, D., Cimatti, A., et al. 2009, A&A, 499, 69
Oke, J. B., & Gunn, J. E. 1983, ApJ, 266, 713
Park, M., Belli, S., Conroy, C., et al. 2023, ApJ, 953, 119
Park, M., Belli, S., Conroy, C., et al. 2024, arXiv:2404.17945
Poggianti, B. M., Calvi, R., Bindoni, D., et al. 2013, ApJ, 762, 77
Schlawin, E., Leisenring, J., Misselt, K., et al. 2020, AJ, 160, 231
Schreiber, C., Glazebrook, K., Nanayakkara, T., et al. 2018, A&A, 618, A85
Scoville, N., Aussel, H., Brusa, M., et al. 2007, ApJS, 172, 1
Setton, D. J., Khullar, G., Miller, T. B., et al. 2024, arXiv:2402.05664

Speagle, J. S. 2020, MNRAS, 493, 3132
Straatman, C. M. S., Labbé, I., Spitler, L. R., et al. 2014, ApJL, 783, L14
Suess, K. A., Kriek, M., Bezanson, R., et al. 2022a, ApJ, 926, 89
Suess, K. A., Kriek, M., Price, S. H., & Barro, G. 2019, ApJ, 877, 103
Suess, K. A., Kriek, M., Price, S. H., & Barro, G. 2020, ApJL, 899, L26
Suess, K. A., Kriek, M., Price, S. H., & Barro, G. 2021, ApJ, 915, 87
Suess, K. A., Leja, J., Johnson, B. D., et al. 2022b, ApJ, 935, 146
Suess, K. A., Williams, C. C., Robertson, B., et al. 2023, ApJL, 956, L42
Tanaka, M., Valentino, F., Toft, S., et al. 2019, ApJL, 885, L34
Toft, S., Zabl, J., Richard, J., et al. 2017, Natur, 546, 510
Treu, T., Auger, M. W., Koopmans, L. V. E., et al. 2010, ApJ, 709, 1195
Valentino, F., Brammer, G., Gould, K. M. L., et al. 2023, ApJ, 947, 20
Valentino, F., Tanaka, M., Davidzon, I., et al. 2020, ApJ, 889, 93
van der Wel, A., Franx, M., van Dokkum, P. G., et al. 2014, ApJ, 788, 28
van der Wel, A., Rix, H.-W., Wuyts, S., et al. 2011, ApJ, 730, 38
van Dokkum, P. G., & Franx, M. 2001, ApJ, 553, 90
van Dokkum, P. G., Franx, M., Kriek, M., et al. 2008, ApJL, 677, L5
van Dokkum, P. G., Whitaker, K. E., Brammer, G., et al. 2010, ApJ, 709, 1018
Weller, E. J., Pacucci, F., Ni, Y., Hernquist, L., & Park, M. 2024, arXiv:2406.02664
Whitaker, K. E., Kriek, M., van Dokkum, P. G., et al. 2012, ApJ, 745, 179
Wild, V., Taj Aldeen, L., Carnall, A., et al. 2020, MNRAS, 494, 529
Wu, P.-F., van der Wel, A., Bezanson, R., et al. 2018, ApJ, 868, 37
Yan, R., & Blanton, M. R. 2012, ApJ, 747, 61
Yan, R., Newman, J. A., Faber, S. M., et al. 2006, ApJ, 648, 281
Yano, M., Kriek, M., van der Wel, A., & Whitaker, K. E. 2016, ApJL, 817, L21
Zhuang, Z., Leethochawalit, N., Kirby, E. N., et al. 2023, ApJ, 948, 132
Zibetti, S., Gallazzi, A., Charlot, S., Pierini, D., & Pasquali, A. 2013, MNRAS, 428, 1479